Remote Sensing of Environment 205 (2018) 85–99

Contents lists available at ScienceDirect

Remote Sensing of Environment

journal homepage: www.elsevier.com/locate/rse

Assessment of the impact of spatial heterogeneity on microwave satellite soil moisture periodic error

Fangni Lei[a,b,*], Wade T. Crow[a], Huanfeng Shen[b], Chun-Hsu Su[c], Thomas R.H. Holmes[d], Robert M. Parinussa[e], Guojie Wang[f]

[a] USDA ARS Hydrology and Remote Sensing Laboratory, Beltsville, MD 20705, USA
[b] School of Resource and Environmental Sciences, Wuhan University, Wuhan, Hubei 430072, China
[c] Department of Infrastructure Engineering, University of Melbourne, Parkville, Victoria 3010, Australia
[d] NASA GSFC Hydrological Sciences Laboratory, Greenbelt, MD 20771, USA
[e] Transmissivity B.V./VanderSat B.V., Space Technology Business Park, Huygenstraat 34, Noordwijk 2201, DK, The Netherlands
[f] School of Geography and Remote Sensing, Nanjing University of Information Science and Technology, Nanjing, Jiangsu 210044, China

ARTICLE INFO

Keywords:
Microwave remote sensing
Satellite-derived soil moisture
Spectral analysis
Periodicity
Spatial heterogeneity

ABSTRACT

An accurate temporal and spatial characterization of errors is required for the efficient processing, evaluation, and assimilation of remotely-sensed surface soil moisture retrievals. However, empirical evidence exists that passive microwave soil moisture retrievals are prone to periodic artifacts which may complicate their application in data assimilation systems (which commonly treat observational errors as being temporally white). In this paper, the link between such temporally-periodic errors and spatial land surface heterogeneity is examined. Both the synthetic experiment and site-specified cases reveal that, when combined with strong spatial heterogeneity, temporal periodicity in satellite sampling patterns (associated with exact repeat intervals of the polar-orbiting satellites) can lead to spurious high frequency spectral peaks in soil moisture retrievals. In addition, the global distribution of the most prominent and consistent 8-day spectral peak in the Advanced Microwave Scanning Radiometer – Earth Observing System soil moisture retrievals is revealed via a peak detection method. Three spatial heterogeneity indicators – based on microwave brightness temperature, land cover types, and long-term averaged vegetation index – are proposed to characterize the degree to which the variability of land surface is capable of inducing periodic error into satellite-based soil moisture retrievals. Regions demonstrating 8-day periodic errors are generally consistent with those exhibiting relatively higher heterogeneity indicators. This implies a causal relationship between spatial land surface heterogeneity and temporal periodic error in remotely-sensed surface soil moisture retrievals.

1. Introduction

Within the past two decades, extensive efforts have been aimed at enhancing remote estimation of surface soil moisture. Currently, several global space-borne soil moisture products are available from a series of satellite-based passive and/or active microwave sensors. The accurate characterization of global satellite-derived soil moisture products is crucial for multiple hydrological (Srivastava et al., 2013; Wagner et al., 2007a), meteorological (Koster et al., 2004; Seneviratne et al., 2010), agricultural (Bolten et al., 2010; Engman, 1991; Lakhankar et al., 2009a), and natural hazardous (Lacava et al., 2005) applications. Especially in hydrological data assimilation community, the inclusion of satellite-based soil moisture observations has drawn great attention for the purposes of catchment rainfall-runoff (Alvarez-Garreton et al., 2014; Crow et al., 2009; Komma et al., 2008) and both continental (Crow and Zhan, 2007; Walker and Houser, 2004) and global-scale (Reichle and Koster, 2005; Reichle et al., 2004, 2007) land surface modeling.

Recently, Su et al. (2013a, 2015) presented a spectrally-based approach for evaluating satellite-derived soil moisture retrievals which builds upon a semi-empirical water balance model and operates in the frequency domain. Based on this approach, they identified periodic error components in passive microwave retrieved soil moisture Level 3 (gridded) retrieval products acquired from both the Advanced Microwave Scanning Radiometer – Earth Observing System (AMSR-E) and the Soil Moisture and Ocean Salinity (SMOS) missions, suggesting the need to consider the presence of temporally-periodic errors when using and/or evaluating such products. Most land data assimilation approaches

---

[*] Corresponding author at: USDA ARS Hydrology and Remote Sensing Laboratory, Beltsville, MD 20705, USA.
E-mail address: leifangni@whu.edu.cn (F. Lei).

https://doi.org/10.1016/j.rse.2017.11.002
Received 6 July 2017; Received in revised form 28 September 2017; Accepted 1 November 2017

are based on an assumption of temporally-white and Gaussian-distributed errors forms (Burgers et al., 1998). Therefore, a thorough examination of soil moisture retrieval error structure is crucial for not only properly describing their error characteristics but also their potential implementation within a land data assimilation system (Crow and Van den Berg, 2010).

Gridded satellite-based soil moisture retrievals are based on the sampling of adjacent footprints within the same orbital overpass. Three commonly used interpolation algorithms are: drop-in-bucket, nearest neighbor, and inverse-distance-squared methods (Chan et al., 2012). The choice of interpolation algorithm affects the effective antenna pattern of the spatial support associated with a particular grid box. For the Soil Moisture Active Passive (SMAP) mission, the averaged half-power beam-width field-of-view (FOV) size of the inverse-distance-squared approach is about 40 km. In addition, radiation outside the half-power beam-width can contribute to the signal – suggesting that the gridded signal may include significant radiance contributions from emitters outside the grid (Jackson et al., 2010). For polar-orbiting satellites with an exact repeat cycle there are periodic variations in the spatial support of individual grids (due to day-to-day variations in the exact footprint-averages underlying each grid cell). Over highly heterogeneous regions, the impact of this periodic sampling may become more pronounced and periodic errors may arise which are related to the periodicity of the sampling pattern.

Additionally, passive microwave observations are potentially contaminated by man-made radio frequency interference (RFI). RFI can obscure (relatively weaker) geophysical emission associated with land source variables like soil moisture (Daganzo-Eusebio et al., 2013; Njoku et al., 2005). In addition to the spatial heterogeneity in natural land surface signals, RFI sources observed over land areas are typically fixed in space (Njoku et al., 2005) which may lead to periodic errors in satellite-based retrievals as these sources are re-sampled periodically. From this point of view, a satellite-derived soil moisture product with consideration of the contributing factor of RFI should be analyzed to expose the origins of periodic errors.

In practice, a simple ad hoc low pass filter (i.e., a 5-day moving average) adopted by Wagner et al. (2007b) and Draper et al. (2009) has been shown to slightly improve the quality of satellite-based soil moisture retrievals. Nonetheless, this empirical method is arbitrary and only effective for dampening very short-term fluctuations (i.e., 2-day periodic errors). Recent experimental studies have shown that analyzing the soil moisture time series in the frequency domain can provide supplementary insights with regard to its conjugate time domain (Katul et al., 2007). For example, Du (2012) used the high-pass Fourier filter to keep small temporal scale soil moisture signals in the directly observed emissivity time series, while filtering out the mixture signals of vegetation phenology in the low frequency component (Moody and Johnson, 2001; Scharlemann et al., 2008) and long-term soil moisture trends. However, such a method requires not only the accurate extraction of high-frequency soil moisture signals from sensor direct observations, but also the availability of an accurate long-term climatology from land surface models or existing satellite-based soil moisture product. On the other hand, Su et al. (2013a) applied a band-stop filter to remove the identifiable stochastic and systematic errors in high-frequency regime and then a low-pass Wiener filter for preserving the long-term temporal mean and variance. This approach is more physically realistic and based on the rationale that small time scale soil moisture dynamics can be simplified into incoming precipitation and water loss process with brown-like spectrum (Katul et al., 2007; Su et al., 2013a).

However, the application of any filter comes at the risk of information loss. For example, when blindly applying the band-stop filter, high-frequency signal components related to rapid soil moisture changes following intense rainfall events can also be attenuated. Therefore, the accurate a priori identification of land surface conditions associated with spurious high frequency resonances is beneficial for efficient and flexible application of the band-stop filter.

To examine the plausible reasons behind the existence of high-frequency peaks and improve our understanding of errors in the satellite-derived soil moisture time series, this study will focus primarily on the most prominent and consistent periodicity (8-day) existing in an AMSR-E soil moisture retrieval product. The spatial distribution of such a periodic error will be inter-compared to measures of land surface spatial heterogeneity. Section 2 presents the satellite-derived soil moisture product from the passive microwave AMSR-E sensor via the Land Parameter Retrieval Model (LPRM) retrieval algorithm, the spectral analysis of soil moisture, and our peak detection method. Three straightforward heterogeneity indicators, based on: microwave brightness temperature, land cover types, and long-term averaged Normalized Difference Vegetation Index (NDVI), are then proposed for characterizing spatial variability along the land surface. Section 3 evaluates the spectral characteristics of soil moisture retrievals and explains their relationship with these heterogeneity indicators. Further discussion of concerns and potential implications is provided in Section 4, and final conclusions are presented in Section 5.

2. Materials and methods

A long-term soil moisture product is necessary in order to robustly investigate periodic errors in satellite-derived soil moisture time series. Among various microwave sensors and missions, the AMSR-E sensor onboard the National Aeronautics and Space Administration (NASA) Aqua provides the longest currently-available source of soil moisture data (i.e., from June 2002 to October 2011) from a single sensor and is therefore the primary focus of this study.

2.1. AMSR-E soil moisture product and LPRM retrieval model

2.1.1. AMSR-E basic information

The AMSR-E sensor was a six-frequency dual-polarized passive microwave radiometer, onboard the NASA Aqua satellite with a 16-day exact repeat cycle. With a sun-synchronous orbit at an altitude of 705 km, AMSR-E scans the Earth's surface at 1:30 a.m. (descending)/1:30 p.m. (ascending) local equator overpass time and an incidence angle of 55°. AMSR-E provided a nearly nine-and-a-half-years long-term measurement time series from June 2002 to October 2011. Among its six microwave frequency bands, the spatial resolutions of footprint measurements at 6.9 GHz (C-band), 10.7 GHz (X-band), and 36.5 GHz (Ka-band) were 74 × 43 km, 51 × 30 km, and 14 × 8 km, respectively (Njoku et al., 2003).

Several soil moisture retrieval algorithms have been developed for AMSR-E brightness temperature (T_B) data. Here, surface soil moisture (~2 cm) and vegetation optical depth are retrieved simultaneously from C-band T_B via the LPRM (see below for further details). In areas with significant RFI such as the contiguous United States (CONUS), Japan, and India, LPRM switches to X-band. Fig. 1a and b shows the distribution maps of bands that have been utilized for soil moisture retrieval. Regardless of the band used, AMSR-E ascending and descending half-orbits are separately re-sampled from their original footprint resolution to a regular quarter degree grid and then processed through LPRM to retrieve soil moisture (see below).

2.1.2. Land parameter retrieval model

LPRM uses a forward modeling optimization procedure to solve a radiative transfer equation without the need for parameter calibration and other biophysical measurements. The physically-based LPRM (De Jeu and Owe, 2003; Meesters et al., 2005; Owe et al., 2001) has been successfully applied to retrieve surface soil moisture from space-borne passive microwave observations including AMSR-E (Owe et al., 2008) and SMOS (De Jeu et al., 2009; Van der Schalie et al., 2015; Van der Schalie et al., 2016). Moreover, the AMSR-E LPRM product has been well-validated with in situ campaigns (Brocca et al., 2011; De Jeu et al.,

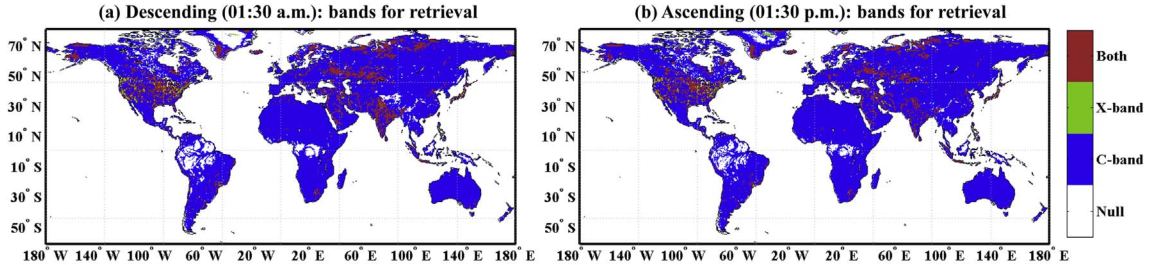

(a) Descending (01:30 a.m.): bands for retrieval

(b) Ascending (01:30 p.m.): bands for retrieval

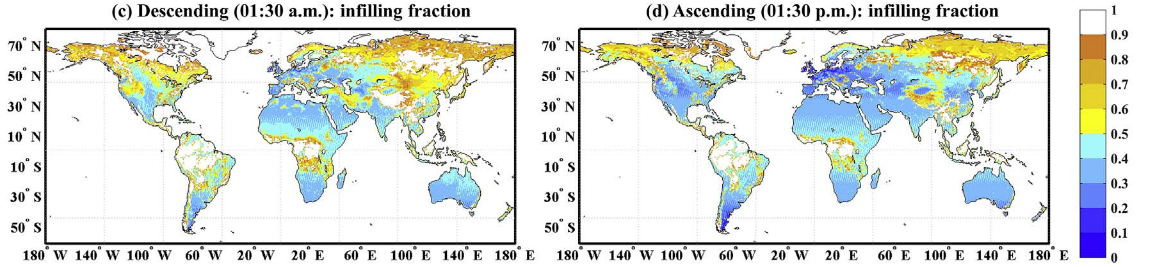

(c) Descending (01:30 a.m.): infilling fraction

(d) Ascending (01:30 p.m.): infilling fraction

Fig. 1. Spatial distribution maps of applied bands for AMSR-E LPRM soil moisture retrieval (upper row) and fraction of in-filled data for the period 2003–2011 (bottom row): (a) and (c) for descending; (b) and (d) for ascending overpasses, respectively.

2008; Draper et al., 2009; Su et al., 2013b) and thoroughly assessed in previous studies (Al-Yaari et al., 2014; Dorigo et al., 2010; Draper et al., 2012; Rebel et al., 2012). Here, version 5 of the AMSR-E LPRM soil moisture product is collected from January 2003 to October 2011.

The LPRM algorithm can simultaneously retrieve surface soil moisture and vegetation optical depth (VOD) from passive microwave observations using both horizontally- and vertically-polarized T_B data. The retrieval scheme is based on solving a radiative transfer model (Mo et al., 1982) via a nonlinear iterative optimization procedure. The radiation emission T_b measured over a land surface with vegetation canopy can be described as

$$T_{b(P)} = T_S e_{r(P)} \Gamma_V + (1-\omega) T_C (1-\Gamma_V) + (1-e_{r(P)})(1-\omega) T_C (1-\Gamma_V)\Gamma_V \tag{1}$$

where the subscript P is H for horizontal or V for vertical polarization, T_S the thermodynamic soil temperature, $e_{r(P)}$ the rough surface emissivity, Γ_V the vegetation transmissivity, ω the single scattering albedo, and T_C the canopy temperature. The above equation represents three terms: the radiation emanated from the underlying soil as attenuated by the canopy, the upward radiation directly from the overlying vegetation, and the downward radiation from the vegetation (reflected by the soil and further attenuated by the vegetation).

The rough surface emissivity is calculated for both polarizations using the emissivity model developed by Wang and Choudhury (1981)

$$e_{r(H)} = 1 - ((1-Q)R_{s(H)} + QR_{s(V)})e^{-h\cos(u)} \tag{2}$$

where Q and h are the polarization mixing factor and empirical roughness, respectively, and both are dimensionless parameters. The smooth surface reflectivity R_s is a function of dielectric constant k and satellite observational incidence angle u and is calculated using the Fresnel equations. Furthermore, the dielectric constant k is estimated via the Wang-Schmugge dielectric mixing model (Wang and Schmugge, 1980). Eq. (2) is written for H polarization emissivity. For V polarization results, the polarization signs should be switched.

The vegetation transmissivity Γ_V is defined in terms of the VOD τ_V and incidence angle u as

$$\Gamma_V = \exp\left(\frac{-\tau_V}{\cos(u)}\right) \tag{3}$$

The VOD τ_V is directly related to the canopy density, or more specifically, the vegetation water content. Derived by Meesters et al. (2005), the VOD is a function of k and the Microwave Polarization Difference Index ($MPDI$)

$$MPDI = \frac{T_{b(V)} - T_{b(H)}}{T_{b(V)} + T_{b(H)}} \tag{4}$$

where $MPDI$ is calculated directly from observed brightness temperatures. By normalizing for temperature dependence, the $MPDI$ becomes more highly-related to the dielectric properties of the radiating body including both the canopy and soil emissions (Owe et al., 2008).

Regarding the thermodynamic conditions of vegetation and soil, a further assumption in the LPRM algorithm is that the soil temperature and canopy temperature are in isothermal equilibrium.

$$T_S = T_c = T \cong aT_{b(V)}^{Ka} + b. \tag{5}$$

For AMSR-E, T is derived from the accompanying Ka-band T_b at V polarization (Holmes et al., 2009). Atmospheric contributions to satellite observed T_B are also taken into account following Owe et al. (2008).

2.2. Ancillary dataset

2.2.1. International Soil Moisture network

The International Soil Moisture network (ISMN) has assembled over 50 operational and experimental soil moisture networks worldwide, providing a global in situ soil moisture database with uniform data format and pre-processing quality flags (Dorigo et al., 2013). While most of the networks are located in northern America and Europe, limited sites in Asia and Australia are also available. Detailed information about the ISMN is reported in Dorigo et al. (2011) and Gruber et al. (2013). The ISMN dataset can be downloaded from http://ismn.geo.tuwien.ac.at.

For direct comparison with AMSR-E LPRM soil moisture product, these sparsely distributed in situ soil moisture records are analyzed in the frequency domain as well. The ISMN soil moisture is originally recorded along with Coordinated Universal Time (UTC) time and has been converted to local solar time. To be consistent with the overpass time of AMSR-E, records are extracted at 02:00 p.m. and 01:00 a.m. for ascending and descending half-orbits, respectively. Observations are masked using the quality flag (identified as 'good' with 'G') and stations located within the same quarter degree box are averaged for simplicity. For example, there are 55 stations from three networks collocated within a quarter degree grid (latitude: 38.375° N, longitude: 120.875° W), namely COSMOS, FLUXNET-AMERIFLUX, and SOILSCAPE.

However, only three stations provided measurements during our study period and are averaged accordingly. Note that the point-scale soil moisture observation cannot fully represent the footprint satellite retrieval and the sampling depth may also introduce differences. Strategies have been proposed for minimizing the systematic differences between ground-based measurement and satellite-based retrievals, such as computing anomalies through subtracting a moving window averaging-based climatology (Dorigo et al., 2015; Gruber et al., 2013). However, since the in situ soil moisture is used only to help identifying spectral peaks in AMSR-E LPRM soil moisture retrievals, these strategies have not been applied here.

2.2.2. Land cover—GlobeLand30

Several global land cover maps derived from multiple satellite sensors are currently available. The sensitivity of microwave emissivity to soil moisture varies with different land cover variables – in particular, vegetation optical depth. High spatial resolution surface land cover maps can thus provide sub-pixel heterogeneity information for coarse resolution soil moisture products. However, the isolation of highly mixed land cover types is cumbersome and beyond the scope of this study. Therefore, the 30-meters high resolution GlobeLand30 dataset, based on Landsat data (Chen et al., 2015) is utilized solely for the visual interpretation of sub-grid spatial heterogeneity finer than the quarter degree resolution AMSR-E LPRM soil moisture retrievals. According to previous independent accuracy assessments, the GlobeLand30 has demonstrated an overall accuracy of over 80% (Brovelli et al., 2015). It can be downloaded from http://globallandcover.com.

2.2.3. Normalized difference vegetation index (NDVI)—MODIS

The Moderate Resolution Imaging Spectroradiometer (MODIS) monthly NDVI (MOD13C2) product is obtained from January 2003 to December 2011. To be consistent with AMSR-E LPRM soil moisture retrievals, it has been spatially-aggregated from its original 0.05° grid to a regular 0.25° resolution. A long-term averaged global NDVI distribution map is then generated by averaging all quarter-degree monthly data. The MOD13C2 dataset can be acquired from https://lpdaac.usgs.gov/dataset_discovery/modis/modis_products_table/mod13c2.

2.2.4. Land cover type—MODIS

In addition to the high resolution land cover from the GlobeLand30 product, a dominant land cover type map at lower spatial resolution (0.05°) is acquired from the MODIS yearly Land Cover Type Climate Modeling Grid (MCD12C1) product in 2011. This product also provides the sub-grid frequency distribution of land cover types. Three classification schemes are included and the primary International Geosphere Biosphere Programme (IGBP) land cover scheme is selected for further analysis. IGBP contains 17 land cover classes and has been re-classified into 9 classes before spatially-aggregated to regular quarter degree (0.25°). They are: Water, Forest, Shrublands, Grasslands, Cultivated Land, Wetlands, Artificial Surfaces, Permanent Snow and Ice, and Bareland. Percentages of difference land cover types are summed for each quarter-degree box and normalized to [0,100]. The MCD12C1 dataset can be downloaded from https://lpdaac. usgs.gov/dataset_discovery/modis/modis_products_table/mcd12c1.

2.3. Spectral frequency analysis and peak detection method

2.3.1. Power spectral density estimation

The dynamics of soil moisture is an outcome of interactions between incoming precipitation, canopy interception, evapotranspiration, surface runoff, lateral flow and groundwater. The near-surface soil moisture time series consists of both a long-term climatology (low frequency) and short-term anomaly (high frequency) components (Entin et al., 2000). The long-term climatology originates from seasonally varying precipitation and solar radiation and can be affected by the vegetation phenology, climate change, and instrument drift for satellite observations. In contrast, the short-term anomalies represent the process of rainfall instances and dry-down events and are valuable for analyzing short-term weather extremes (Katul et al., 2007; Wu and Dickinson, 2004). However, this short-term information is usually contaminated by observational noises and systematic errors. Here, we focus on the periodic error in the high-frequency regime which may be introduced by the satellite orbiting pattern and/or gridding approach.

Following the approach of Su et al. (2013a, 2015), the power spectral density (PSD, in unit of m^6/m^6 24 h/rad) of AMSR-E LPRM soil moisture retrievals at a given grid is estimated using the Welch's averaged modified periodogram method. This method computes a modified periodogram for each temporal segment separated by a moving Hamming window and averages over all estimates to produce a single PSD. Note that the size of Hamming window can play a role in determining the PSD estimation. Wider Hamming windows tend to produce higher spectral resolution in the estimated PSD but greater uncertainty in the amplitude estimation, while shorter windows provide coarser spectral resolution but with lower uncertainty in amplitude. The impact of Hamming window size on key results will be clarified when describing the peak detection method in Section 2.3.4.

Another issue with PSD estimation is satellite overpass time. AMSR-E has an ascending half-orbit at 1:30 p.m. and descending half-orbit at 1:30 a.m. Considering that the FOV and near-surface thermal conditions (more specifically, the temperature contrast across the soil-vegetation-air interface) are quite different for these two half-orbits, soil moisture retrievals from ascending and descending overpasses have been separately analyzed with periodic temporal sampling along a 24 h interval.

In applying the Fourier transform to stationary time series, most standard PSD estimation algorithms – including Welch's method – require an evenly sampled dataset in time. However, temporal data gaps in passive microwave satellite-derived soil moisture product are inevitable – primarily due to the satellite orbits, dense vegetation, RFI contamination, and masking for frozen soil conditions. In this particular case, AMSR-E LPRM soil moisture retrievals are masked if the complementary VOD levels exceeded 0.8—a level at which the soil radiation is substantially masked out by the canopy (Owe and Holmes, 2008; De Jeu et al., 2008; Parinussa et al., 2011). Further masking has been conducted for grids with significant RFI contamination (Li et al., 2004) and for frozen soil conditions. In order to produce evenly-spaced data after the application of this masking, the 1-D Discrete Cosine Transform (DCT) method (Garcia, 2010) is applied for infilling missing values in the AMSR-E LPRM soil moisture time series. In this study, only grids with less than 365 observations during the 9-years experiment period (11%) are omitted to preserve sufficient spatial coverage for global analysis with indication of highly in-filled regions. The impact of applying a more stringent minimum coverage threshold is discussed below. Fig. 1c and d show the fraction of in-filled data in the AMSR-E LPRM soil moisture product for both descending and ascending retrievals. Due to the generally warmer surface conditions during the ascending (01:30 p.m.) half-orbit (Holmes et al., 2015), the fraction of data gaps in descending overpasses is slightly higher than their ascending counterparts. Additional discussion and an assessment of the infilling method can be found in Section 4.2 and section A of the supporting materials.

2.3.2. Spectrum characteristics of soil moisture time series

Fig. 2 shows the AMSR-E LPRM and ISMN in situ soil moisture time series from January 2003 to October 2011 for a single 0.25° grid (latitude: 38.375° N, longitude: 120.875° W). Corresponding PSDs are estimated with two Hamming window sizes (i.e., 1.0 and 8.8 in units of year).

According to Katul et al. (2007), the soil water balance model dictates that the soil moisture time series exhibits a Brownian spectrum with more energy at lower frequency and a decrease in power with

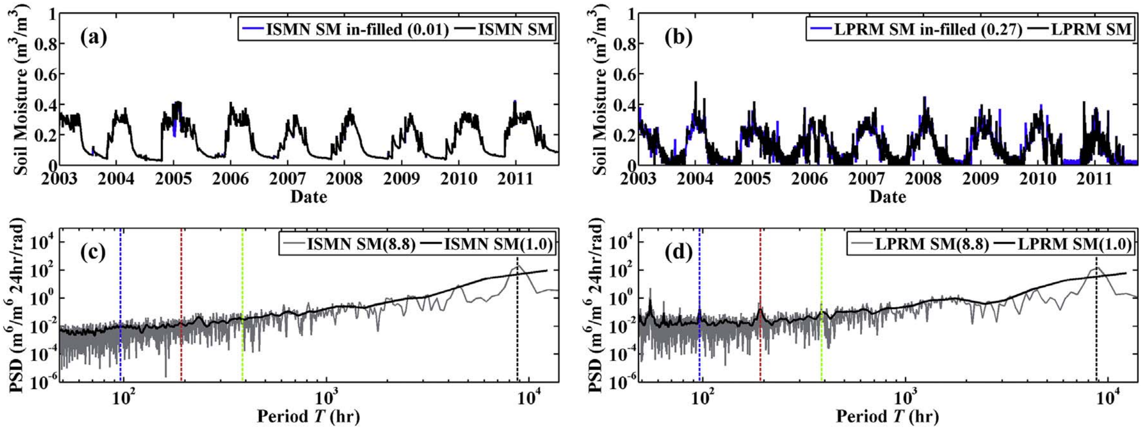

Fig. 2. The soil moisture time series (a and b) and corresponding power spectral density (PSD, c and d) of both ISMN in situ and AMSR-E LPRM soil moisture data at the ascending overpass time (01:30 p.m.). The infilling fractions of soil moisture data are shown in the brackets and the Hamming window sizes for PSD estimation inside the brackets are in units of year. From left to right, the dotted vertical lines represent periods at 4-day (blue), 8-day (red), 16-day (green), and 365-day (black). (For interpretation of the references to color in this figure legend, the reader is referred to the web version of this article.)

increasing frequency (Fig. 2c). Comparing the PSDs of footprint AMSR-E LPRM soil moisture retrievals and point-scale in situ observations, significant discrepancies exist at high frequencies. In particular, the relatively flat power distributions of AMSR-E LPRM soil moisture for $T < 10^3$ h reflect high-frequency noise, which can be introduced by various short-term stochastic processes contributing to retrieval errors (Su et al., 2013a). Note that – based on a thorough exploration over various grids with in situ soil moisture observations – the grid demonstrated here is representative for a spectral comparison between ground-based measurements and satellite-derived soil moisture retrievals.

Importantly, several distinct resonant peaks with periods ranging between 2 and 16 days are sitting on the AMSR-E flat noise floor (Fig. 2d). Given the lack of known physical processes capable of producing such harmonics, these peaks are likely spurious signals characterized by periodic increases in power with these time intervals. Without consideration of the long-term satellite orbit drift, the repeat cycle of AMSR-E is 16 days which means that the sensor observes exactly the same region every 16 days. Within this 16-day period, there are periodic variations in the locations of antenna footprints sampled to capture a grid-cell mean (as shown in Fig. 3). Our hypothesis is that this kind of periodic sampling pattern can generate spectral peaks within highly heterogeneous regions. If true, it implies that spectral peaks can be connected to strong – and temporally stable – patterns of land surface heterogeneity.

2.3.3. Examining the occurrence of periodic errors

To further facilitate the physical interpretation of the occurrence of high-frequency peaks, a simplistic synthetic experiment monitoring the periodic sampling pattern of satellite swaths over different land cover characteristics has been conducted following the approach illustrated in Fig. 4. In particular, an Antecedent Precipitation Index (API) model is applied to generate synthetic soil moisture $SM_{t,i}$ (mm, in a dimension of water depth) for each sub-grid i at time t

$$SM_{t,i} = \gamma SM_{t-1,i} + P_t \qquad i = 1, \ldots, n \tag{6}$$

where γ is a dimensionless API loss coefficient and assumed to be a constant value as 0.95; n is the total number of sub-grids which is set to 9 (3-by-3), and P_t (mm) represents the daily accumulation depth of random rainfall expressed in dimensions of water depth and generated from the exponential distribution with mean of 25 mm.

In total, there are five synthetic scenarios (see Fig. 4). The synthetic "True" soil moisture is generated directly through the API model without any assumed observational error, while mean-zero Gaussian distributed random observational error with a standard deviation of 10 mm is added to the other four cases. With the consideration of

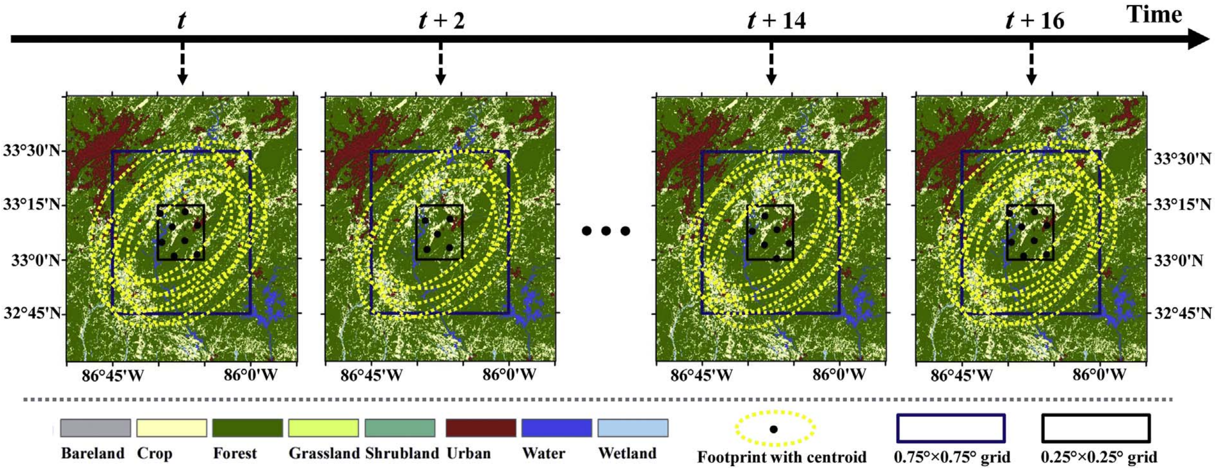

Fig. 3. An illustration of the time-varying effective spatial support for a single quarter degree grid (centered at 33.125° N, 86.375° W and outlined with a black square) where multiple adjacent footprints (yellow dotted ellipses) within the same orbital overpass are averaged. The background land cover maps are projected in World Geodetic System (WGS) 1984 Universal Transverse Mercator (UTM) zone 16 North system. Comparing time t and $t + 16$, the satellite observes exactly the same region. (For interpretation of the references to color in this figure legend, the reader is referred to the web version of this article.)

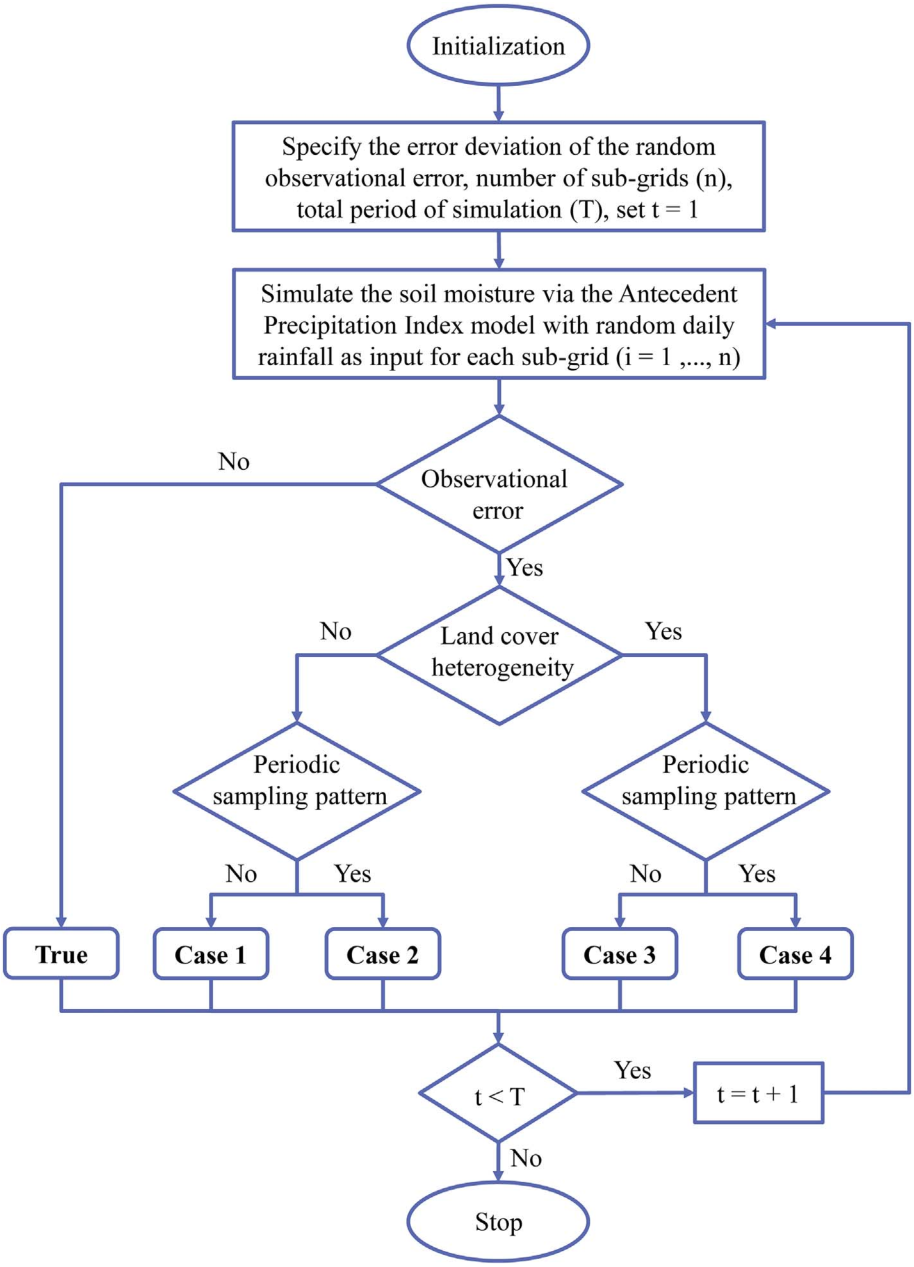

Fig. 4. Flowchart of synthetic experiments which examine the combined impact of land surface heterogeneity and periodic orbital sampling pattern on producing spectral harmonics.

spatial heterogeneity, a long-term bias in soil moisture within the 3-by-3 grid box is set up as a random pattern from a mean-zero normal distribution with a standard deviation of 20 mm. This long-term bias is meant to represent the systematic land cover and/or soil physical property variations. Furthermore, the periodic sampling pattern of satellite footprints is constructed by repeating equally-weighted averaging with different combinations of sub-grids (to account for the drop-in-bucket method use in the AMSR-E LPRM product). In accordance with AMSR-E, the repeat cycle is set to 16-days. Through the combination of these two conditions, four experiments are generated (see Fig. 4). Here, the differences in mean and standard deviation settings among precipitation, soil moisture observational error and long-term bias only represent their scaling differences and proportionally rescaling these statistical moments does not affect presented results. Before the spectral frequency analysis, five synthetic soil moisture time series (four Cases and "True") are normalized respectively from their original climatology to be mean-zero with a standard deviation of one. These synthetically-generated results will be used to enhance our understanding of peak-generating processes within our real-data analysis. Results from these synthetic experiments will be presented in Section 3.1.

2.3.4. Detection of 8-day periodic error

With a Brownian spectrum of soil moisture, the increase in power with decreasing frequency may hinder detection of 16-day peaks in cases where the true soil moisture signal is stronger than the 16-day resonance. In addition, spectral peak features in higher frequencies can be difficult to be distinguished from the high-frequency noise. Therefore, despite the fact that AMSR-E LPRM soil moisture retrievals demonstrate several spectral resonances, we will focus on 8-day peaks as they represent the most prominent and consistent periodic signal. Detailed peak detection procedures are described below.

To start, the PSD estimations of AMSR-E LPRM soil moisture product are conducted using the Welch's method with different Hamming window sizes. As stated earlier, the window size determines the amplitude accuracy and frequency resolution of the PSD. To reach a compromise between these two factors, and provide sufficient support for detecting periodicity in high frequency, the window size is varied between 270 and 360 days at 10-day intervals. Thus, for each grid, there are ten separate estimates of PSD. These PSDs and corresponding frequency series are then transformed into logarithm space for further analysis. Polynomial interpolation is used to remove the background Brownian shape of PSD, allowing for more accurate detection of the peaks. For detecting the most prominent and consistent 8-day peaks, two thresholds are employed: a) the minimum peak height is no less than 3-sigma (standard deviation) of the de-trended PSD estimations; and b) the 8-day peaks are repeatedly detected by at least 5 times (out of the 10 Hamming window sizes considered at each grid). In addition, the same peak detection approach is applied for AMSR-E brightness temperature T_B-derived parameters as described in the following Section 2.4.1.

2.4. Land surface heterogeneity indicator

The land surface characteristics are extremely variable in both space and time. Our strategy is based on applying the best available global descriptions of land surface characteristics from both microwave and visible/near-infrared remote sensing and comparing these patterns to maps of 8-day spectral peak presence. Naturally, all heterogeneity descriptions have resolution limitations which prevent them from capturing all sub-pixel scale heterogeneity (Lakhankar et al., 2009b).

2.4.1. T_B-derived heterogeneity indicator

The AMSR-E T_B data are re-sampled onto regular quarter degree grid using a drop-in-bucket approach. Quarter degree grid-scale averages are acquired by averaging all footprints – across various scans and swath cycles – whose geographic centers fall within a grid box for a given day. Thereby, the spatial coverage of the effective radiating body can extend beyond the boundaries of each grid box. In fact, according to Jackson et al. (2010), the main contribution of radiation can come from a 0.75° × 0.75° box centered at each quarter degree grid. Therefore, mirroring the land surface parameterization of the LPRM algorithm, a T_B-derived heterogeneity indicator (TB-HI) is proposed to characterize the spatial heterogeneity of the underlying land surface (within a centered 0.75° × 0.75° box) for several adjoining satellite footprints within the same orbital overpass

$$H_{3\times3}^{TB} = H_{3\times3}^{MPDI} + H_{3\times3}^{MWE} + H_{3\times3}^{TEMP} \tag{7}$$

where

$$H_{3\times3}^{MPDI} = std\,[\log(MPDI)_{i,j}] \equiv std\left[\log\left(\frac{1}{N}\Sigma_{t=1}^{N}\frac{T_{B(V),t}^{C} - T_{B(H),t}^{C}}{T_{B(V),t}^{C} + T_{B(H),t}^{C}}\right)_{i,j}\right]\ i,j \sim(1,2,3) \tag{8}$$

$$H_{3\times3}^{MWE} = std\,[\log(MWE)_{i,j}] \equiv std\left[\log\left(\frac{1}{N}\sum_{t=1}^{N}\frac{T_{B(H),t}^{C}}{T_{B(V),t}^{Ka}}\right)_{i,j}\right]\ i,j\sim(1,2,3) \tag{9}$$

$$H_{3\times3}^{TEMP} = std\left[\log\left(\frac{1}{N}\Sigma_{t=1}^{N}T_{B(V),t}^{Ka}\right)_{i,j}\right]\ i,j\sim(1,2,3) \tag{10}$$

and $std[\sim]$ represents the mathematic operation of calculating standard deviation for a 3 × 3 box (i.e., 0.75° × 0.75°). In Eqs. (8)–(10), i and j are the grid index within the 3 × 3 box, and N is the total number of sampled time steps. ${H_{3\times3}}^{MPDI}$ is calculated based on the AMSR-E C-band T_B data and can be a reflection of both the soil and canopy information (Owe et al., 2001). Moreover, the effective emissivity ($MWE = T_{B(P)}/T$) is used in Eq. (9) to capture the heterogeneity in emissivity while the Ka-band T_B at V represents the effective surface temperature T. The spatial variation of temperature is also taken into account using Eq. (10). For simplicity, fixed values of $MPDI$, MWE, and ${T_{B(V)}}^{Ka}$ are assigned to water bodies: $MPDI = 0.2$ (Chen et al., 2011), $MWE = 0.5$ (Grody, 1993; Weng, 2010), ${T_{B(V)}}^{Ka} = 220$ (Lin et al., 1998). The ranges of these heterogeneity components are slightly different, thus global normalization has been conducted for each component and ${H_{3\times3}}^{TB}$ (unit-less) is further normalized into [0, 100] after arithmetic summation. Note that this heterogeneity indicator is computed directly from the AMSR-E observed T_B data without any other auxiliary biophysical information sources and can be adapted to other microwave satellite or retrieval algorithms as well. For example, C-band ${T_{B(P)}}^{C}$ could be replaced with L-band ${T_{B(P)}}^{L}$ acquired from the SMOS and SMAP missions, while surface temperature data could also potentially be derived from land surface model output.

2.4.2. NDVI-derived heterogeneity indicator

Vegetation canopy plays an important role in observing and retrieving soil moisture from space-borne platforms (Jackson et al., 1982). NDVI is a simple index of vegetation density which can be applied for depicting the land surface characteristics. To take into account the canopy, a straightforward NDVI-derived heterogeneity indicator (VI-HI) is proposed with a form similar to TB-HI

$$H_{3\times3}^{VI} = std\left[\left(\frac{1}{N}\Sigma_{t=1}^{N}NDVI_t\right)_{i,j}\right]\ i,j\sim(1,2,3) \tag{11}$$

where the standard deviation ($std[\sim]$) of NDVI is calculated for a 3 × 3 box centered at each quarter degree grid. This indicator characterizes the spatial variability of vegetation density over the average main-beam FOV of AMSR-E.

2.4.3. Land cover-derived heterogeneity indicator

Different land cover types can demonstrate distinct physical characteristics with varying temporal climatology. Regions with various land cover types can be quite heterogeneous with regard to satellite-based soil moisture retrieval. Therefore, a land cover-derived heterogeneity indicator (LC-HI) is defined as the number of individual land cover types contained within a single 0.75° × 0.75° box for each quarter degree grid

$$H_{3\times3}^{LC} = |(\langle LC_k^{Perc} \geq 10\rangle \cup \langle 10 > LC_{Water}^{Perc} > 0\rangle)_{i,j}|\quad k\sim(1,9)\quad i,j\sim(1,2,3) \tag{12}$$

where $|\sim|$ denotes the cardinality operator, ${LC_k}^{Perc}$ represents the grid area in percent classified as land cover type k (out of nine classes), and ${LC_{Water}}^{Perc}$is the percentage classified as Water. Open water, with its high dielectric constant, has a profound impact on the microwave emission and even small fractions of open water may greatly alter the T_B observations (Loew, 2008). In this case, LC-HI will increase 1 if there is open water within the 3 × 3 box. The other land cover classes are only taken into account when their percentages are larger than 10%.

3. Results

Our main interest is examining the most prominent and consistent spectral peaks generated from AMSR-E's periodic sampling pattern and the relationship between theses peaks and the spatial heterogeneity of the corresponding land surface. To physically explore the occurrence of high frequency spectral peaks, we begin by presenting both a simple synthetic experiment (see Section 2.3.3) and a detailed site-specified analysis using real observations. Subsequently, the global distribution of the 8-day periodic errors, and their relationship with the spatial heterogeneity indicators introduced in Section 2.4, is presented.

3.1. Synthetic experiments

Fig. 5 demonstrates the PSD estimations of five synthetic soil moisture time series (as described in Section 2.3.3). Compared to the

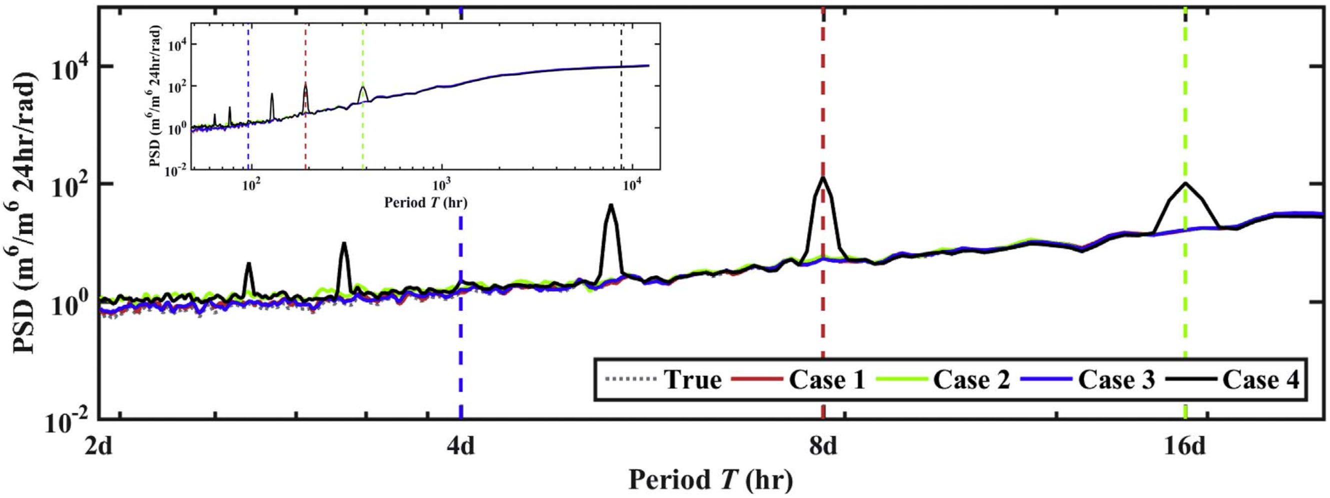

Fig. 5. High-frequency PSD for soil moisture time series generated by the synthetic "True" case and the synthetic "satellite-based" Cases 1–4. The Hamming window size is set equal to 365 days. The entire PSDs (including lower-frequency components) are shown in the upper left corner. From left to right, the colored dashed vertical lines represent 4-day, 8-day, 16-day, and 365-day periods. Note that the PSDs of the "True" case and Cases 1–3 are virtually indistinguishable.

"True" scenario, both Case 1 and Case 3 show quite similar spectral characteristics suggesting that the land cover heterogeneity alone cannot lead to high-frequency peaks without periodic sampling pattern. While both Case 2 and Case 4 exhibit a moderate noise floor over the "True" soil moisture for periods between 2- and 4-days. Particularly, significant frequency peaks are exposed when the periodic sampling pattern is combined with spatial heterogeneity in Case 4. The results suggest that, in the absence of either the spatial heterogeneity or periodic sampling patterns, high frequency peaks cannot be produced.

Additionally, the influence of different re-gridding methods on the occurrence of spectral peaks has been explored. All PSD estimations of three re-gridded soil moisture time series have shown notable spectral peaks, indicating that the peaks are result for a combination of periodic sampling patterns and stable spatial heterogeneity – regardless of exact re-gridding method applied (see section B of the supporting materials for further discussion).

3.2. Site-specified analysis

Fig. 6a and f show land cover maps for two arbitrary 0.75° × 0.75° grids within North America (hereafter referred as to Sites A and B). Also shown are the enlarged 3-year time series (from January 2004 to December 2006) for AMSR-E LPRM soil moisture and corresponding spectral analysis within each 0.25° × 0.25° grid located at the center of these 0.75° × 0.75° grids – as outlined by the black boxes. Both sites in Fig. 6 represent highly heterogeneous land surface conditions. From the GlobeLand30 land cover map of Site A (latitude: 38.875° N, longitude: 121.125° W), a highly heterogeneous satellite orbit overpassing region can be observed with large portions of forest and urban land cover. Meanwhile, the fractions of water bodies, crop, grassland, and shrubland land cover types are also non-trivial with a relatively clear spatial pattern (Fig. 6a). In particular, the urban area is mainly located in the lower-left corner, while forest covers upper-right corner. Grassland is mixed with crop, shrubland and water bodies. A strong negative trend in vegetation density from upper-right to lower-left can be observed.

The soil moisture time series for Site A (Fig. 6b and c) demonstrates a relatively strong seasonal climatology with values varying from 0.01 to 0.5 (m^3/m^3). AMSR-E LPRM soil moisture retrieval for each quarter degree grid is generated based as the mean of all swath data whose footprint centers fall within that particular grid (Owe et al., 2008). The soil moisture record manifests several significant spectral resonances – including a significant 8-day peak. Moreover, 4-day and 16-day peaks are also conspicuous for both overpasses. Given their uses in LPRM retrievals, the T_B-derived *MPDI* and *MWE* are also analyzed in frequency domain. Similarly, an 8-day peak in *MPDI* appears in both half-orbits – suggesting that the spectral peaks in soil moisture retrievals can be traced back to the *MPDI*. However, the probability of occurrence and the relative amplitude of spectral peaks in soil moisture and *MPDI* are not exactly the same for each peak. On the other hand, the PSDs of *MWE* also show 8-day and 4-day spectral peaks for the ascending overpass (Fig. 6e) and a 4-day peak for the descending overpass (Fig. 6d). Therefore, within Site A, strong spatial heterogeneity in land cover appears capable of generating soil moisture spectral peaks associated with the satellite orbiting cycle.

Likewise, Site B (latitude: 34.125° N, longitude: 87.125° W) exhibits strong spatial land cover heterogeneity (Fig. 6f). Specifically, forest covers the north-western regions and is mixed with crops and grasslands. Small patches of urban and water bodies are sparsely distributed throughout the scene. The soil moisture time series values range from 0.01 to 0.7 (m^3/m^3). Despite a lack of strong large-scale spatial variation, this site also demonstrates heterogeneous land surface characteristics with different land cover types thoroughly mixed with each other. Both the ascending and descending soil moisture time series contain 8-day peaks in the frequency domain (Fig. 6i and j) with the ascending peak more prominent. For the descending overpass, the more equivalent thermodynamic conditions are beneficial for applying the LPRM soil moisture retrieval algorithm. A significant 8-day peak in the descending *MPDI* does not lead to a comparable peak in the soil moisture retrievals (Fig. 6i). Also, fewer peaks are observed in the PSDs of *MWE* compared to Site A. Other factors such as the vegetation density and soil and canopy effective temperatures in the retrieval process can play a role in determining the retrieved soil moisture. Specifically, the microwave radiation emitted from water bodies is quite different from other land cover types and can strongly impact soil moisture retrievals (Gouweleeuw et al., 2012).

In contrast to the relatively heterogeneous sites examined in Fig. 6, Fig. 7 looks at two spatially homogeneous sites (Sites C and D). The two sites are dominated by grassland and crop cover, respectively. The coverage fractions of other land cover types are relatively negligible. Both soil moisture time series depict a relatively small seasonal climatology compared to Fig. 6 without the orbiting cycle-related spectral peaks. Also, no prominent peaks are observed from the PSDs of both T_B-derived *MPDI* and *MWE*.

By investigating four different sites with various spatial coverages of land cover types, a possible link between spectral peaks of retrieved soil moisture and the directly observed T_B can be inferred. The spatial

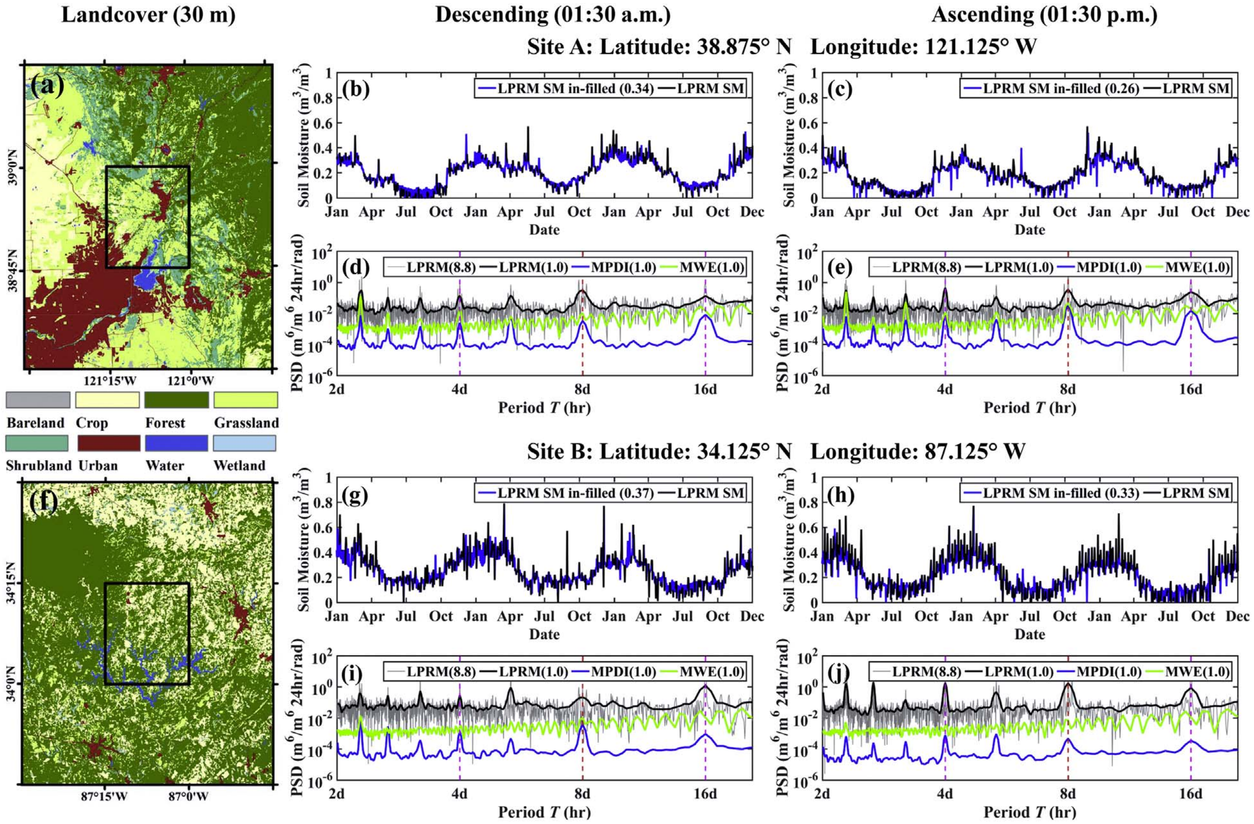

Fig. 6. Site-specified demonstrations of high resolution land cover (a and f), descending (b, d, g, and i) and ascending (c, e, h, and j) AMSR-E LPRM soil moisture and brightness temperature (T_B). Each land cover map depicts a 0.75° × 0.75° grid centered at different locations (Sites A and B) with the black box outlines the 0.25° × 0.25° grid. Maps are projected in WGS 1984 UTM coordinate system and latitudes and longitudes of sites are shown as well. Enlargements of the 3-years (from January 2004 to December 2006) time series of soil moisture retrievals are included for each site and the infilling fractions are shown in the brackets. The spectral analyses are conducted for AMSR-E LPRM soil moisture retrievals and T_B-derived Microwave Polarization Difference Index (*MPDI*) and Microwave Emissivity (*MWE*). The Hamming window sizes for PSD estimations are indicated by units of year in the brackets. Dotted vertical lines represent three periods at 4-day, 8-day, and 16-day.

heterogeneity combined with systematic orbiting cycle can lead to the spectral peaks in *MPDI* and thus soil moisture retrievals.

3.3. Global distribution of spectral peaks

While interesting, results in Figs. 6 and 7 are clearly anecdotal in nature. In order to examine more general tendencies, global distributions of the 8-day spectral peaks in LPRM AMSR-E soil moisture retrievals are plotted in Fig. 8 for both descending and ascending overpasses. Regions with high (over 50%) infilling fractions (Fig. 1c and d) are indicated with different color settings for grids with or without 8-day spectral peaks.

Generally speaking, the spatial distribution of spectral peaks is similar for both half-orbits. However, relatively more peaks are found in the ascending half-orbit – 20% versus 17% of the total land grids over the globe. Both descending and ascending overpasses have demonstrated notable spectral peaks over densely-vegetated areas of Eastern CONUS. On the other hand, there exist moderately different distributions of peaks over Western CONUS. Note that significant discrepancies of near-surface (soil, canopy and air) vertically thermal profiles can be observed between the AMSR-E nighttime descending (01:30 a.m.) and daytime ascending (01:30 p.m.) overpasses. During nighttime, near-surface isothermal conditions benefit the retrieval of soil moisture from brightness temperature observations with higher accuracy (Jackson et al., 2010), yielding fewer spurious spectral peaks in the descending overpass.

Comparing regions with high infilling fractions (blue and dark brown in Fig. 8) to those with low infilling fractions (red and light brown), indicates that the frequency of peak is lower for areas with a larger amount of infillings (i.e., 12% versus 24%, and 13% versus 20% for ascending and descending overpasses, respectively). With increased infilling fractions, more in-filled data are included for the peak detection, which leads to an increase in the missed detection of peaks (please refer to section A of the supporting materials for more details). As a result, there is no indication that peaks are spuriously created by the infilling process. Instead, the infilling actually appears to obscure the expression of peaks.

Additionally, comparing Figs. 8 and 1a or b, the presence of RFI may impact the occurrence of spectral peaks. See Section 4.1 for additional discussion on this point.

Fig. 9 shows results for a comparable peak analysis conducted for the T_B-derived *MPDI* and *MWE*. As depicted, both descending (Fig. 9a and c) and ascending (Fig. 9b and d) half-orbits have a similar spatial distribution pattern with regard to *MPDI* or *MWE*. Overall spatial patterns of 8-day peaks in *MPDI* are comparable with that in soil moisture retrievals. However, 8-day peaks in *MPDI* are relatively more common than soil moisture peaks in Fig. 8. Comparing to (relatively dynamic) soil moisture values, *MPDI* is more likely to respond to temporally-stable land surface elements, such as land cover type and vegetation density.

In contrast, *MWE* maps in Fig. 9 demonstrate relatively fewer peaks than soil moisture in Fig. 8. *MWE* as a function of several varying variables, including water content and soil salinity, changes rapidly over land surface (Prigent et al., 2006). More specifically, the intensity and duration of precipitation events modulate the land surface emissivity (Ferraro et al., 2013). Consequently, *MWE* does not generally show strong and persistent land surface heterogeneity over the 16-day exact repeat cycle of AMSR-E sensor. Taken as a whole, Fig. 9 suggests

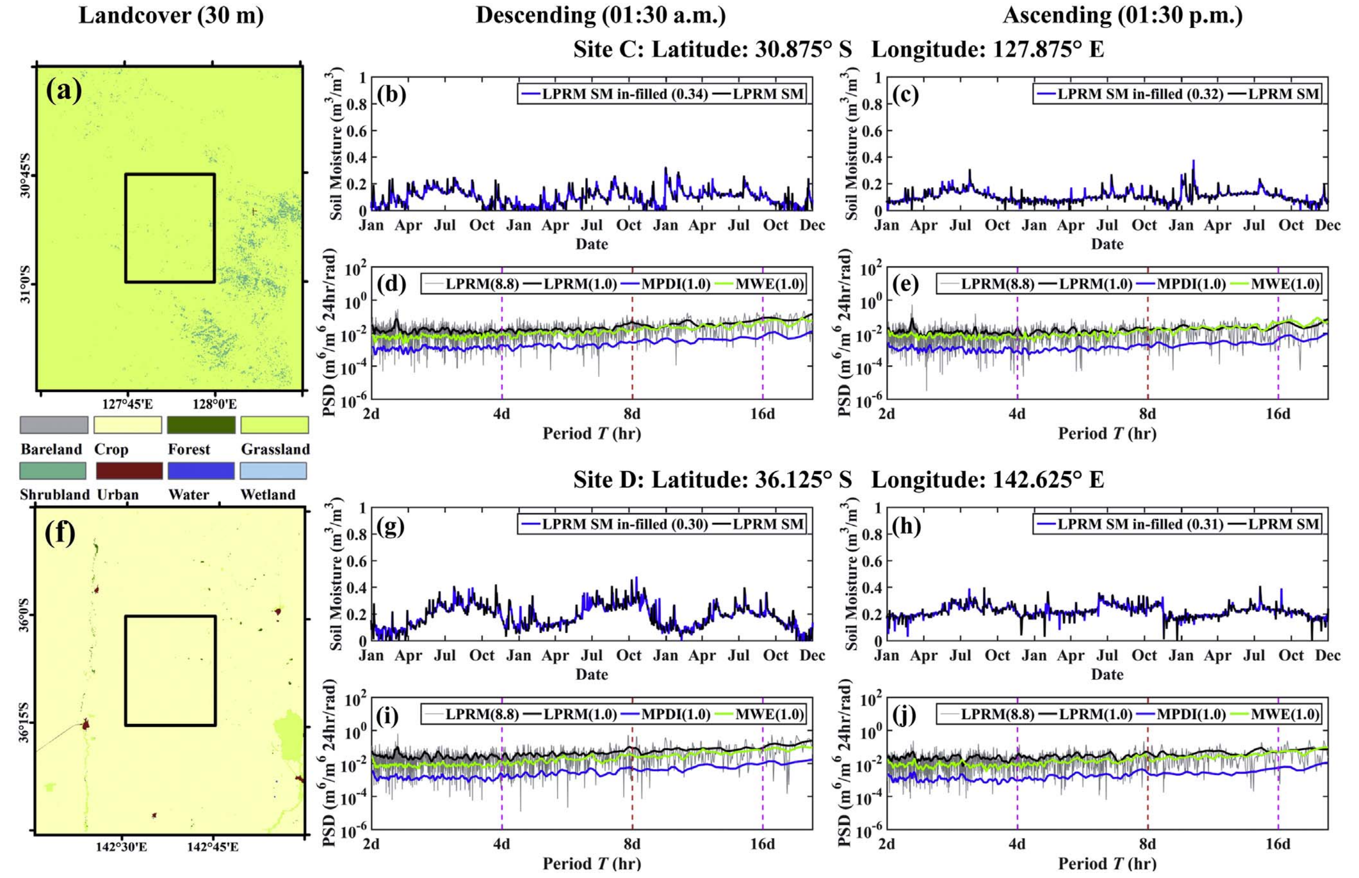

Fig. 7. Same with Fig. 6 except for Sites C and D.

that *MPDI* heterogeneity represents the primary source of periodicity in LPRM soil moisture retrievals.

3.4. Relating the 8-day periodic error to spatial heterogeneity

To explore the relationship between the presence of an 8-day spectral peak in soil moisture retrievals and the land surface spatial heterogeneity, three heterogeneity indicators are computed for each

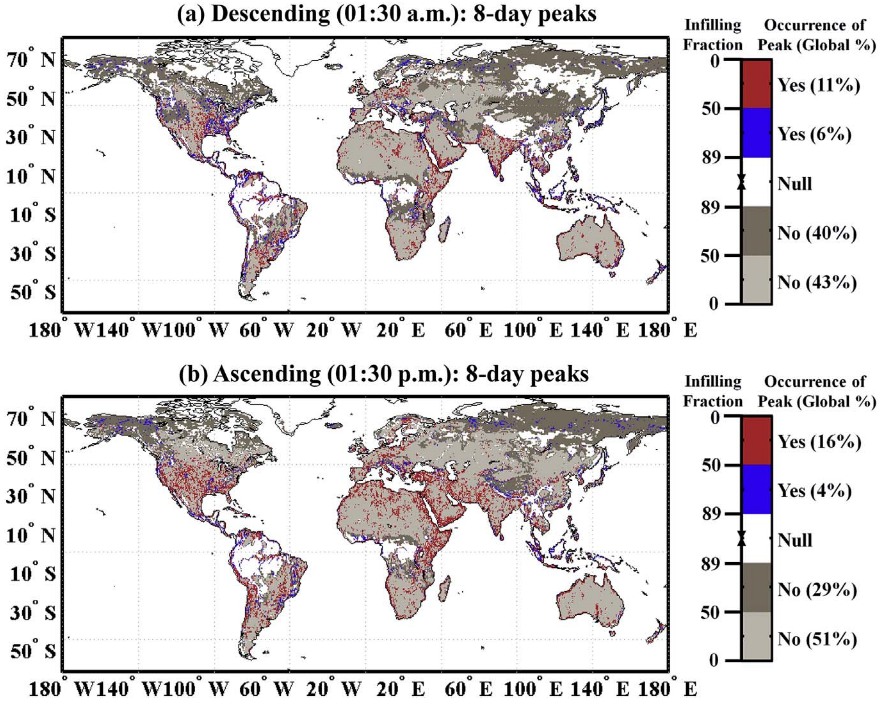

Fig. 8. Global distribution maps of 8-day spectral peaks in the AMSR-E LPRM soil moisture product for both (a) descending and (b) ascending half-orbits. Regions with in-filled data below 50% (89%: over 365 observations during the 9-years experiment period) are shown in light (dark) brown. Accordingly, grids with peaks are indicated in blue or red. The percentages of grids with/without 8-day peaks in regard to the total grids for both descending and ascending overpasses are computed, respectively. (For interpretation of the references to color in this figure legend, the reader is referred to the web version of this article.)

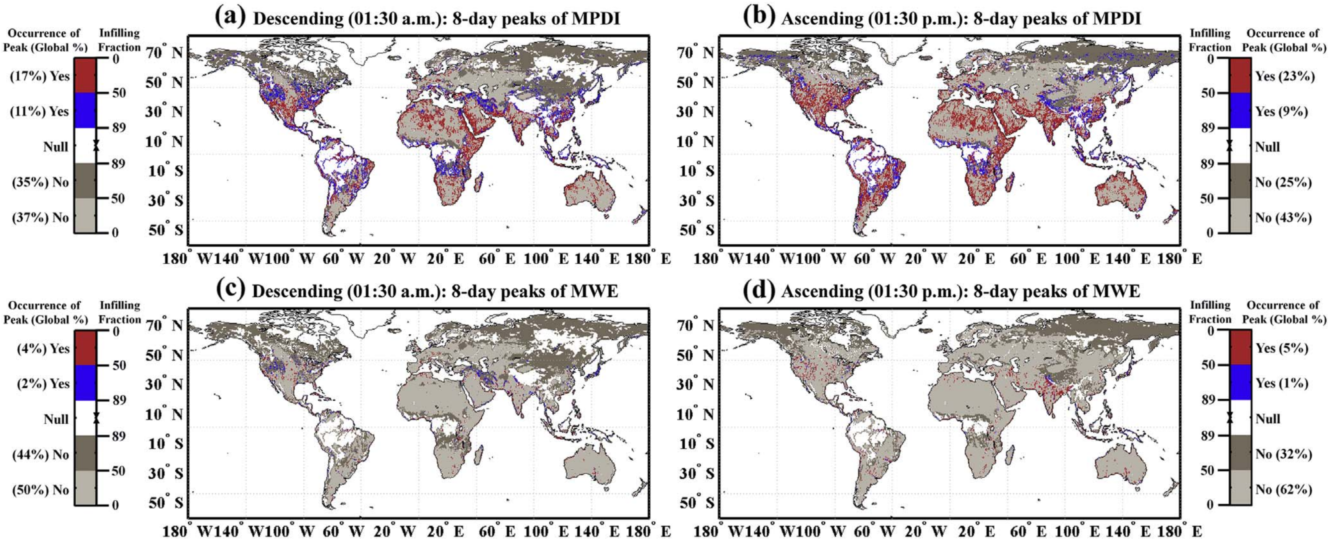

Fig. 9. Global distribution maps of 8-day spectral peaks in AMSR-E T_B-derived *MPDI* (a and b) and *MWE* (c and d) for both descending and ascending half-orbits. Color setting is same as Fig. 8 and percentages of grids with/without 8-day peaks is shown in the legend.

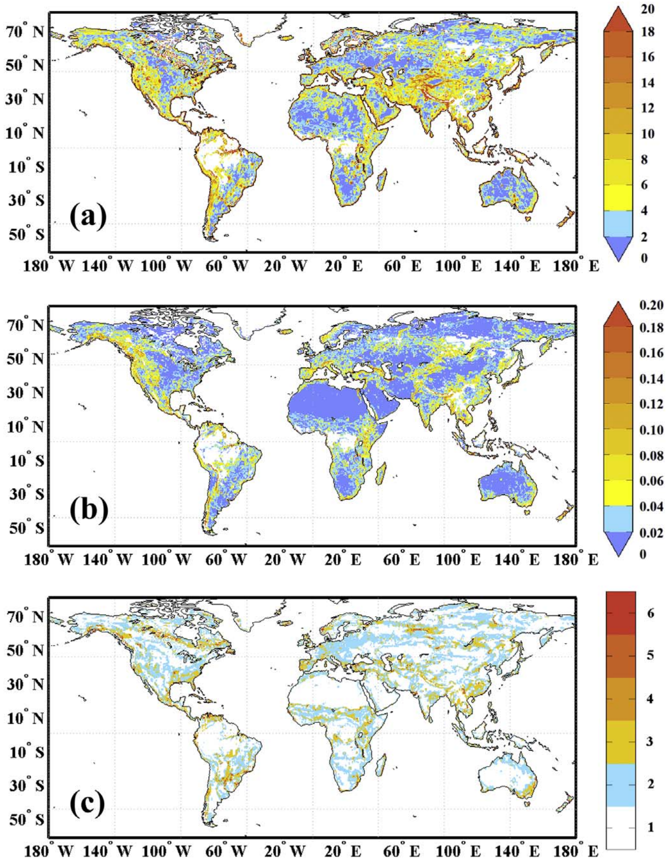

Fig. 10. Global maps of three heterogeneity indicators calculated from: (a) AMSR-E T_B observations (TB-HI), (b) long-term averaged vegetation index and (VI-HI), and (c) land cover types (LC-HI).

Table 1
Global means and medians of three heterogeneity indicators under two conditions: with or without 8-day peaks identified in soil moisture retrievals. Statistics for both descending (01:30 a.m.) and ascending (01:30 p.m.) half-orbits are calculated. Data in parentheses are computed for regions with infilling fraction smaller than 50%.

Indicator	Descending		Ascending		Valid range
	Yes	No	Yes	No	
Mean					
TB-HI	15.30 (13.01)	5.70 (4.89)	12.98 (11.45)	6.18 (4.91)	[0 100]
VI-HI	0.06 (0.05)	0.03 (0.03)	0.05 (0.05)	0.03 (0.03)	[0 0.4]
LC-HI	2.09 (2.07)	1.66 (1.62)	1.97 (1.94)	1.70 (1.63)	[1 6]
Median					
TB-HI	7.29 (6.91)	3.20 (3.09)	6.38 (6.21)	3.22 (3.01)	[0 100]
VI-HI	0.04 (0.04)	0.02 (0.02)	0.03 (0.03)	0.02 (0.02)	[0 0.4]
LC-HI	2 (2)	1 (1)	2 (2)	2 (1)	[1 6]

quarter degree grid (see Section 2.4 above). Fig. 10 shows global maps of these three heterogeneity indicators, namely TB-HI, VI-HI, and LC-HI. For each map, larger values indicate larger amounts of land surface spatial heterogeneity although the valid ranges are different for each indicator (see Table 1 for details).

The three maps emphasize different aspects of spatial heterogeneity which results in different distributions of indicator values. Nevertheless, the spatial distribution of high heterogeneity indicators is generally consistent with the occurrence of 8-day peaks in the AMSR-E LPRM soil moisture product (Fig. 8). Regions such as the Amazon and the Tibetan Plateau have demonstrated a significant relationship that grids with 8-day peaks have extremely high TB-HI (Fig. 10a). Likewise, in western CONUS, South America, South Africa, and India, a relatively close link can be observed. Along the west coast of South America and over West Central Africa, a comparable distribution of high VI-HI and grids with 8-day peak is observable (Fig. 10b). LC-HI also shows some high values for central Southern Africa (Fig. 10c) where 8-day peaks are frequently detected.

Both VI-HI and LC-HI fail to capture the information over non-vegetated landscapes, e.g., North Africa and the Arabian Peninsula. These two indicators are based solely on relatively coarse-resolution land cover characteristics and cannot fully represent the land surface variability. Instead, other factors not captured in the indices, such as soil texture and roughness, may play a primary role in determining the heterogeneity for low-vegetated regions.

Table 1 shows the global mean and median values for each of the three indicators, both for grids with and without 8-day peaks. Under all circumstances, grids with the 8-day peak are generally associated with relative higher mean and median values of the heterogeneity indicators. This further suggests that the occurrence of spectral peaks can be

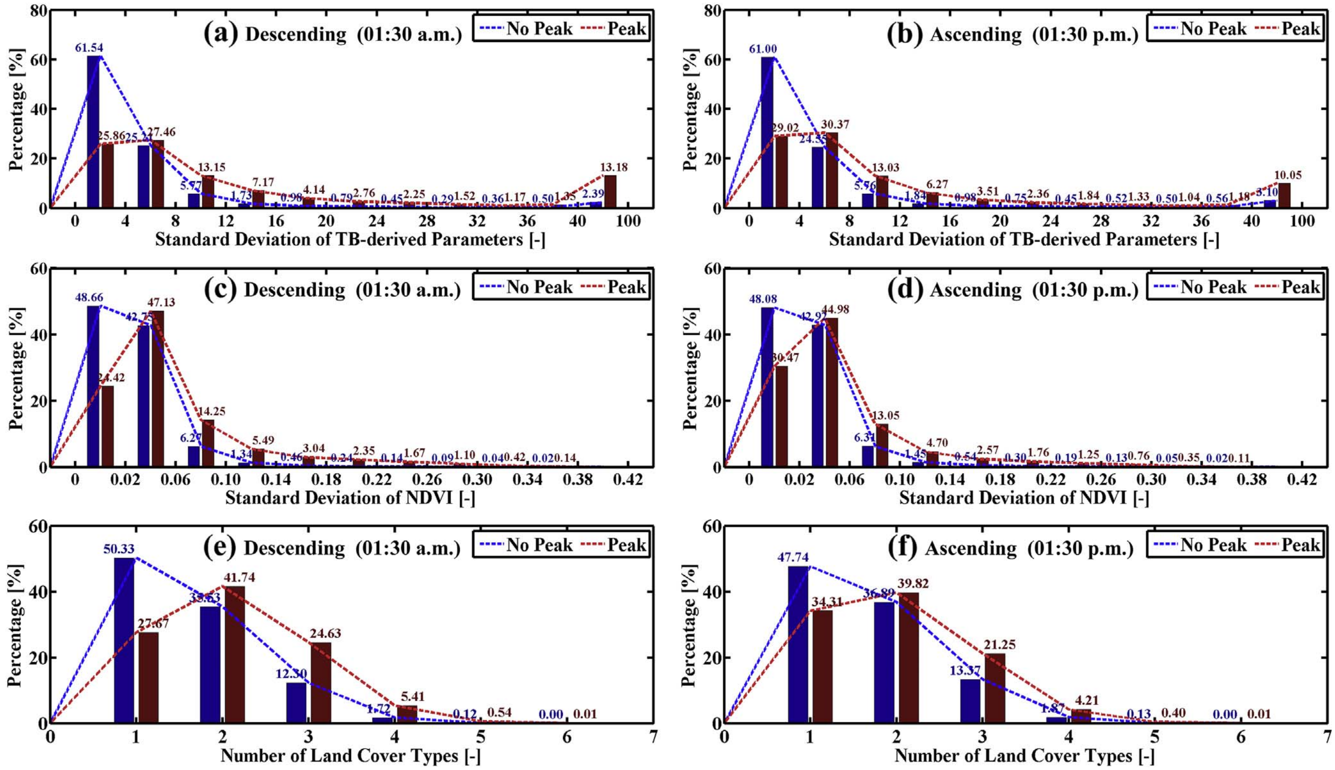

Fig. 11. Histograms of three heterogeneity indicators for grids with or without 8-day peaks. Descending and ascending overpasses are separately processed over the globe.

related to the land surface spatial heterogeneity. In addition, Fig. 11 shows the normalized histograms (to [0,100]) of three indicators over the globe for grids with or without 8-day peaks. Descending and ascending overpasses are separately processed and the statistical hypothesis test (Wilcoxon-Mann-Whitney test) has been performed for six scenarios. All test results indicate that the median of the indicator for grids with peaks is greater than that for grids without peaks at a 0.001 significance level. This suggests a statistically significant capability for the three heterogeneity indicators to characterize regions with strong land surface variability.

For grid cells without peaks, nearly half has the lowest level of spatial heterogeneity indicators. For example, 61.54% (61.00%) of grids without peaks in descending (ascending) overpass has a TB-HI smaller than 4 (Fig. 11a and 11). Conversely, over 74% (71%) of grids with peaks in descending (ascending) overpass has a TB-HI larger than 4. Similar contrasts can be found for the other indicators. Overall, grids with higher values of the heterogeneity indicators are more likely to contain 8-day peaks in soil moisture retrievals.

4. Discussion

The accurate characterization of errors in remotely sensed soil moisture products is important for satellite calibration/validation activities and the development of optimized assimilation approach for integrating retrievals with hydrologic modeling. In contrast to the common assumption of temporally white errors, Su et al. (2013a) demonstrated that AMSR-E and SMOS gridded soil moisture products over Australia depict spectral resonances suggesting the existence of periodic errors. Here, we expanded the time series spectral analysis in Su et al. (2013a) to a global domain and explored the physical origins of these periodic errors.

Through the synthetic experiments, the periodic errors can be linked to the combination of the periodic sampling patterns and the land surface spatial heterogeneity (Fig. 5). Results of AMSR-E LPRM soil moisture product further presented a link of spectral peaks existing in T_B-derived *MPDI* and soil moisture retrievals. More specifically, that spatial heterogeneity within the satellite's field-of-view can lead to the periodicity in *MPDI* estimates which are then transmitted into soil moisture retrievals. As demonstrated in Fig. 8, LPRM soil moisture derived from both ascending and descending overpasses demonstrate significant 8-day spectral peaks along coastal areas and some regions with water bodies, e.g., the Amazon floodplain and areas of central Australia with ephemeral salt lakes. In addition, regions with spatially-heterogeneous land cover (e.g., eastern CONUS, South America, Western Europe, Peninsular India, and southern China) appear more likely to have the 8-day peaks.

4.1. Potential role of radio frequency interference

The AMSR-E LPRM soil moisture product is a combined product which has utilized both C- and X-band T_B to retrieve soil moisture. The C-band frequency, which is theoretically more sensitive to variations in soil moisture, is treated as the primary data source. However, over regions with high RFI contaminations, the retrieval method switches from C- to X-band (shown in Fig. 1a and b). This strategy can largely mitigate the influence of strong and spatio-temporally constant RFI. Fig. 6 shows an illustration of RFI impact at two heterogeneous sites with contrasting land surface characteristics. For Site A, urban area covers a large portion of the $0.75^\circ \times 0.75^\circ$ grid and only X-band T_B has been utilized for retrieving soil moisture. While the RFI impact has been eliminated to a great extent, spectral peaks are detected from the corresponding soil moisture retrievals (Fig. 6d and e). In contrast, without significant RFI at Site B, C-band T_B has been applied and periodic errors still exist (as shown in Fig. 6i and j). This suggests that the periodicity found in AMSR-E LPRM soil moisture product cannot be attributed to RFI alone.

On the other hand, in addition to the T_B-derived heterogeneity indicators, another two indicators which are computed from independent MODIS vegetation index and land cover type information will not reflect RFI information. As depicted in Fig. 11, VI-HI and LC-HI have demonstrated statistically significant skills in characterizing land surface heterogeneity. Via a pre-defined threshold for each heterogeneity indicator, VI-HI and LC-HI can partially differentiate grids with peaks from those without peaks indicating the causal relationship between spatial variability of natural land surface and the occurrence of peaks.

Nevertheless, similarities between RFI map (Fig. 7a in Njoku et al., 2005) and ascending spectral peak map (Fig. 8b) can be observed, for example over CONUS and the western Arabian Peninsula. Note that the RFI detection method is based on the spectral difference between the 6.9 and 10.7 GHz channels and a threshold should be assigned to determine whether RFI exists or not (Li et al., 2004). Consequently, if RFI is of low-level or spatially/temporally intermittent (which is often the real case), it might escape the detection. Moreover, regions with RFI contaminations are often close to urban areas, where transitions in architecture and building density, vegetation, and anthropogenic activity are thoroughly mixed (Cadenasso et al., 2007). Under such circumstance, a high heterogeneity of land surface characteristics (including both natural and artificial features) can be observed over these regions and thus lead to more spectral peaks in soil moisture retrievals. Therefore, RFI can intensify the land surface heterogeneity and increase the probability of occurrence of spectral peaks in satellite-derived soil moisture retrievals.

4.2. Impact of the infilling method

To conduct the spectral analysis, the 1-D infilling method was performed to achieve evenly-spaced observations. Given that the infilling method is based on statistics sampled from the entire time series, the results retain the autocorrelation structure of soil moisture in the high frequency domain but in-filled values are smoothed with low frequency climatology for significant gaps (Wang et al., 2012). Comparing Fig. 1c or d with Fig. 8, no obvious spatial correlation between the infilling fraction and existence of 8-day peak can be observed – suggesting that our infilling approach does not lead to the spurious production of spectral peaks. Aside from high latitudes near the pole where the interpolation fraction is extremely large and there is less chance of having 8-day peaks, in most regions with small infilling fractions, such as Western Europe, South America, Africa, and Australia, there is no evidence that the gap infilling has an impact on the frequency of peak occurrence.

In order to further examine this point, a synthetic control test has been conducted to explore the impact of infilling fraction. Details can refer to section A in the supporting materials. The results demonstrated that, as expected, the accuracy of in-filled soil moisture time series gradually decreases with increasing infilling fractions. However, no spurious spectral peaks will be introduced by the infilling method, suggesting that any spectral peaks detected in the in-filled soil moisture data are present in the original time series. Further studies may explore alternative PSD estimation approaches such as the Lomb-Scargle periodogram (Lomb, 1976; Scargle, 1982) or wavelet transform-based method (Foster, 1996) which do not require evenly-spaced observations.

4.3. Potential applications

Results in Fig. 8 identified significant periodic error components in existing soil moisture remote sensing product and globally mapped their distribution. Removing such systematic error components is a critical goal of satellite calibration activities and could potentially aid in the development of optimized gridding and processing procedures. A global identification map of such periodic errors would also be beneficial for identifying highly heterogeneous regions for the targeted application of a band-stop filter (Su et al., 2013a, 2015) for removing the systematic periodic errors in short-term satellite-derived soil moisture products.

For short-term available satellite-based soil moisture products, the baseline of applying the band-stop filtering is to apply it indiscriminately to every grid cell. In this case, the majority of grids without significant frequency peaks can be over-smoothed (because over 80% of global grid cells lack 8-day soil moisture peaks). Moreover, spatial heterogeneity may similarly affect other satellite-based products, particularly when they have similar orbital configurations and retrieval inputs as AMSR-E LPRM. For satellite records which are too short for PSD estimation, one option is to utilize a peak distribution map generated from the long-term (9 + year) AMSR-E soil moisture time series as the criterion for identifying heterogeneous regions in which to apply a band-stop filter.

5. Conclusions

Via a synthetic experiment imitating the periodic sampling pattern of polar-orbiting satellite swaths over various land cover characteristics, the combination of spatial land surface heterogeneity and periodic orbital sampling pattern are linked to periodic errors in remotely-sensed soil moisture retrievals (Fig. 5). In data real cases utilizing AMSR-E LPRM soil moisture retrievals, site-specific studies demonstrate that the satellite repeat cycle can generate a periodicity in the T_B-derived *MPDI* and corresponding LPRM soil moisture retrievals (Figs. 6 and 7). By applying the peak detection method, global distribution maps of 8-day peaks in AMSR-E LPRM soil moisture retrievals and T_B-derived *MPDI* and *MWE* can be generated. Comparisons between these maps show strong evidence that the satellite orbiting cycle-related spectral peaks are more likely to occur in highly-heterogeneous land regions (Figs. 8 and 9). The conclusion is intuitive to understand. The re-gridding method of satellite observations is usually based on a selection of all footprints within the same orbital overpass covering the given grid. Due to the progression of the satellite orbit, the track changes from day to day with an exact repeat cycle and thus introduces the periodic errors into the sampling over regions with large land surface heterogeneity.

The global identification of the periodic error is of importance for the data assimilation community and will also support the development of improved soil moisture re-gridding and post-processing methods. To globally correlate the occurrence of such spectral peaks with heterogeneity in land surface characteristics, three heterogeneity indicators have been proposed and shown their statistically significant capability in detecting high-heterogeneous regions with 8-day peaks (Fig. 10, Fig. 11, and Table 1). The association between heterogeneity indicators and the occurrence of 8-day periodic errors is compelling evidence of the causal link between land surface spatial heterogeneity and the periodic errors in satellite-based re-gridded soil moisture product.

While these heterogeneity indicators have demonstrated statistically significant skills at a global scale, they do not predict all peaks (and predict some peaks which to not occur). As a result, further refinement of these indicators is necessary to make them of immediate value in an operational retrieval and/or data assimilation context. Nevertheless, results presented here represent an important first step in this direction as both synthetic and real data results provide clear evidence of a general link between land surface spatial heterogeneity and the occurrence of periodic errors in AMSR-E soil moisture retrievals. Additionally, other PSD estimation approaches and soil moisture products using different retrieval algorithms (Kim et al., 2015), such as the JAXA product retrieved by Japan Aerospace Exploration Agency, should be included in follow-on analyses.

Acknowledgement

The authors would like to acknowledge the contribution of Land Parameter Retrieval Model development team, all scientists that provided their ground-based measurements with the International Soil Moisture Network, the GlobeLand30 research group for sharing the high resolution land cover data, the MODIS science team for providing accessible data products. The authors would also like to thank the four anonymous reviewers for their constructive comments. This work was supported by the Cross-disciplinary Collaborative Teams Program for Science, Technology and Innovation of the Chinese Academy of Sciences.

Appendix A. Supplementary data

Supplementary data to this article can be found online at https://doi.org/10.1016/j.rse.2017.11.002.

References

Alvarez-Garreton, C., Ryu, D., Western, A., Crow, W., Robertson, D., 2014. The impacts of assimilating satellite soil moisture into a rainfall–runoff model in a semi-arid catchment. J. Hydrol. 519, 2763–2774.

Al-Yaari, A., Wigneron, J.P., Ducharne, A., Kerr, Y., De Rosnay, P., De Jeu, R., Govind, A., Al Bitar, A., Albergel, C., Munoz-Sabater, J., 2014. Global-scale evaluation of two satellite-based passive microwave soil moisture datasets (SMOS and AMSR-E) with respect to land data assimilation system estimates. Remote Sens. Environ. 149, 181–195.

Bolten, J.D., Crow, W.T., Zhan, X., Jackson, T.J., Reynolds, C.A., 2010. Evaluating the utility of remotely sensed soil moisture retrievals for operational agricultural drought monitoring. IEEE Journal of Selected Topics in Applied Earth Observations and Remote Sensing 3 (1), 57–66.

Brocca, L., Hasenauer, S., Lacava, T., Melone, F., Moramarco, T., Wagner, W., Dorigo, W., Matgen, P., Martínez-Fernández, J., Llorens, P., 2011. Soil moisture estimation through ASCAT and AMSR-E sensors: an intercomparison and validation study across Europe. Remote Sens. Environ. 115 (12), 3390–3408.

Brovelli, M.A., Molinari, M.E., Hussein, E., Chen, J., Li, R., 2015. The first comprehensive accuracy assessment of GlobeLand30 at a national level: methodology and results. Remote Sens. 7 (4), 4191–4212.

Burgers, G., Jan van Leeuwen, P., Evensen, G., 1998. Analysis scheme in the ensemble Kalman filter. Mon. Weather Rev. 126 (6), 1719–1724.

Cadenasso, M.L., Pickett, S.T., Schwarz, K., 2007. Spatial heterogeneity in urban ecosystems: reconceptualizing land cover and a framework for classification. Front. Ecol. Environ. 5 (2), 80–88.

Chan, S., Njoku, E., Colliander, A., 2012. SMAP Algorithm Theoretical Basis Document: L1C Radiometer Data Product, Tech. Rep. SMAP Project, JPL D-53053. Jet Propulsion Laboratory, Pasadena, CA.

Chen, J., Chen, J., Liao, A., Cao, X., Chen, L., Chen, X., He, C., Han, G., Peng, S., Lu, M., 2015. Global land cover mapping at 30m resolution: a POK-based operational approach. ISPRS J. Photogramm. Remote Sens. 103, 7–27.

Chen, S.S., Chen, X.Z., Chen, W.Q., Su, Y.X., Li, D., 2011. A simple retrieval method of land surface temperature from AMSR-E passive microwave data—a case study over southern China during the strong snow disaster of 2008. Int. J. Appl. Earth Obs. Geoinf. 13 (1), 140–151.

Crow, W.T., Huffman, G.J., Bindlish, R., Jackson, T.J., 2009. Improving satellite-based rainfall accumulation estimates using spaceborne surface soil moisture retrievals. J. Hydrometeorol. 10 (1), 199–212.

Crow, W.T., Van den Berg, M., 2010. An improved approach for estimating observation and model error parameters in soil moisture data assimilation. Water Resour. Res. 46 (12), W12519.

Crow, W.T., Zhan, X., 2007. Continental-scale evaluation of remotely sensed soil moisture products. IEEE Geosci. Remote Sens. Lett. 4 (3), 451–455.

Daganzo-Eusebio, E., Oliva, R., Kerr, Y.H., Nieto, S., Richaume, P., Mecklenburg, S.M., 2013. SMOS radiometer in the 1400–1427-MHz passive band: impact of the RFI environment and approach to its mitigation and cancellation. IEEE Trans. Geosci. Remote Sens. 51 (10), 4999–5007.

De Jeu, R., Wagner, W., Holmes, T., Dolman, A., Van De Giesen, N., Friesen, J., 2008. Global soil moisture patterns observed by space borne microwave radiometers and scatterometers. Surv. Geophys. 29 (4), 399–420.

De Jeu, R.A., Holmes, T.R., Panciera, R., Walker, J.P., 2009. Parameterization of the land parameter retrieval model for L-band observations using the NAFE'05 data set. IEEE Geosci. Remote Sens. Lett. 6 (4), 630–634.

De Jeu, R.A.M., Owe, M., 2003. Further validation of a new methodology for surface moisture and vegetation optical depth retrieval. Int. J. Remote Sens. 24 (22), 4559–4578.

Dorigo, W., Scipal, K., Parinussa, R., Liu, Y., Wagner, W., De Jeu, R., Naeimi, V., 2010. Error characterisation of global active and passive microwave soil moisture datasets. Hydrol. Earth Syst. Sci. 14 (12), 2605–2616.

Dorigo, W., Wagner, W., Hohensinn, R., Hahn, S., Paulik, C., Xaver, A., Gruber, A., Drusch, M., Mecklenburg, S., Oevelen, P.v., 2011. The International Soil Moisture Network: a data hosting facility for global in situ soil moisture measurements. Hydrol. Earth Syst. Sci. 15 (5), 1675–1698.

Dorigo, W.A., Gruber, A., De Jeu, R.A.M., Wagner, W., Stacke, T., Loew, A., Albergel, C., Brocca, L., Chung, D., Parinussa, R.M., Kidd, R., 2015. Evaluation of the ESA CCI soil moisture product using ground-based observations. Remote Sens. Environ. 162, 380–395.

Dorigo, W.A., Xaver, A., Vreugdenhil, M., Gruber, A., Hegyiová, A., Sanchis-Dufau, A.D., Zamojski, D., Cordes, C., Wagner, W., Drusch, M., 2013. Global automated quality control of in situ soil moisture data from the International Soil Moisture Network. Vadose Zone J. 12 (3) (vzj2012-0097).

Draper, C., Walker, J., Steinle, P., De Jeu, R., Holmes, T., 2009. An evaluation of AMSR-E derived soil moisture over Australia. Remote Sens. Environ. 113 (4), 703–710.

Draper, C.S., Reichle, R.H., De Lannoy, G.J.M., Liu, Q., 2012. Assimilation of passive and active microwave soil moisture retrievals. Geophys. Res. Lett. 39 (4), L04401.

Du, J., 2012. A method to improve satellite soil moisture retrievals based on Fourier analysis. Geophys. Res. Lett. 39 (15), L15404.

Engman, E.T., 1991. Applications of microwave remote sensing of soil moisture for water resources and agriculture. Remote Sens. Environ. 35 (2), 213–226.

Entin, J.K., Robock, A., Vinnikov, K.Y., Hollinger, S.E., Liu, S., Namkhai, A., 2000. Temporal and spatial scales of observed soil moisture variations in the extratropics. J. Geophys. Res. 105 (D9), 11865–11877.

Ferraro, R.R., Peters-Lidard, C.D., Hernandez, C., Turk, F.J., Aires, F., Prigent, C., Lin, X., Boukabara, S.A., Furuzawa, F.A., Gopalan, K., Harrison, K.W., 2013. An evaluation of microwave land surface emissivities over the continental United States to benefit GPM-era precipitation algorithms. IEEE Trans. Geosci. Remote Sens. 51 (1), 378–398.

Foster, G., 1996. Wavelets for period analysis of unevenly sampled time series. Astron. J. 112 (4), 1709–1729.

Garcia, D., 2010. Robust smoothing of gridded data in one and higher dimensions with missing values. Computational Statistics and Data Analysis 54 (4), 1167–1178.

Gouweleeuw, B., van Dijk, A., Guerschman, J.P., Dyce, P., Owe, M., 2012. Space-based passive microwave soil moisture retrievals and the correction for a dynamic open water fraction. Hydrol. Earth Syst. Sci. 16 (6), 1635–1645.

Grody, N.C., 1993. Remote sensing of the atmosphere from satellites using microwave radiometry. In: Janssen, Michael A. (Ed.), Atmospheric Remote Sensing by Microwave Radiometry, pp. 259–334.

Gruber, A., Dorigo, W., Zwieback, S., Xaver, A., Wagner, W., 2013. Characterizing coarse-scale representativeness of in situ soil moisture measurements from the International Soil Moisture Network. Vadose Zone J. 12 (2) (vzj2012-0170).

Holmes, T., De Jeu, R., Owe, M., Dolman, A., 2009. Land surface temperature from Ka band (37 GHz) passive microwave observations. J. Geophys. Res.-Atmos. 114, D04113.

Holmes, T.R.H., Crow, W.T., Hain, C., Anderson, M.C., Kustas, W.P., 2015. Diurnal temperature cycle as observed by thermal infrared and microwave radiometers. Remote Sens. Environ. 158, 110–125.

Jackson, T.J., Cosh, M.H., Bindlish, R., Starks, P.J., Bosch, D.D., Seyfried, M., Goodrich, D.C., Moran, M.S., Du, J., 2010. Validation of advanced microwave scanning radiometer soil moisture products. IEEE Trans. Geosci. Remote Sens. 48 (12), 4256–4272.

Jackson, T.J., Schmugge, T.J., Wang, J.R., 1982. Passive microwave sensing of soil moisture under vegetation canopies. Water Resour. Res. 18 (4), 1137–1142.

Katul, G.G., Porporato, A., Daly, E., Oishi, A.C., Kim, H.S., Stoy, P.C., Juang, J.Y., Siqueira, M.B., 2007. On the spectrum of soil moisture from hourly to interannual scales. Water Resour. Res. 43 (5), 1–10.

Kim, S., Liu, Y., Johnson, F.M., Parinussa, R.M., Sharma, A., 2015. A global comparison of alternate AMSR2 soil moisture products: why do they differ? Remote Sens. Environ. 161, 43–62.

Komma, J., Blöschl, G., Reszler, C., 2008. Soil moisture updating by Ensemble Kalman filtering in real-time flood forecasting. J. Hydrol. 357 (3), 228–242.

Koster, R.D., Dirmeyer, P.A., Guo, Z., Bonan, G., Chan, E., Cox, P., Gordon, C., Kanae, S., Kowalczyk, E., Lawrence, D., 2004. Regions of strong coupling between soil moisture and precipitation. Science 305 (5687), 1138–1140.

Lacava, T., Cuomo, V., Di Leo, E.V., Pergola, N., Romano, F., Tramutoli, V., 2005. Improving soil wetness variations monitoring from passive microwave satellite data: the case of April 2000 Hungary flood. Remote Sens. Environ. 96 (2), 135–148.

Lakhankar, T., Ghedira, H., Temimi, M., Azar, A.E., Khanbilvardi, R., 2009b. Effect of land cover heterogeneity on soil moisture retrieval using active microwave remote sensing data. Remote Sens. 1 (2), 80–91.

Lakhankar, T., Krakauer, N., Khanbilvardi, R., 2009a. Applications of microwave remote sensing of soil moisture for agricultural applications. International Journal of Terraspace Science and Engineering 2 (1), 81–91.

Li, L., Njoku, E.G., Im, E., Chang, P.S., Germain, K.S., 2004. A preliminary survey of radio-frequency interference over the US in Aqua AMSR-E data. IEEE Trans. Geosci. Remote Sens. 42 (2), 380–390.

Lin, B., Wielicki, B., Minnis, P., Rossow, W., 1998. Estimation of water cloud properties from satellite microwave, infrared and visible measurements in oceanic environments: 1. Microwave brightness temperature simulations. J. Geophys. Res.-Atmos. 103 (D4), 3873–3886.

Loew, A., 2008. Impact of surface heterogeneity on surface soil moisture retrievals from passive microwave data at the regional scale: the upper Danube case. Remote Sens. Environ. 112 (1), 231–248.

Lomb, N.R., 1976. Least-squares frequency analysis of unequally spaced data. Astrophysics and Space Science 39 (2), 447–462.

Meesters, A.G., De Jeu, R.A., Owe, M., 2005. Analytical derivation of the vegetation optical depth from the microwave polarization difference index. IEEE Geosci. Remote Sens. Lett. 2 (2), 121–123.

Mo, T., Choudhury, B., Schmugge, T., Wang, J., Jackson, T., 1982. A model for microwave emission from vegetation-covered fields. J. Geophys. Res. Oceans 87 (C13), 11229–11237.

Moody, A., Johnson, D.M., 2001. Land-surface phenologies from AVHRR using the discrete Fourier transform. Remote Sens. Environ. 75 (3), 305–323.

Njoku, E.G., Ashcroft, P., Chan, T.K., Li, L., 2005. Global survey and statistics of radio-frequency interference in AMSR-E land observations. IEEE Trans. Geosci. Remote Sens. 43 (5), 938–947.

Njoku, E.G., Jackson, T.J., Lakshmi, V., Chan, T.K., Nghiem, S.V., 2003. Soil moisture retrieval from AMSR-E. IEEE Trans. Geosci. Remote Sens. 41 (2), 215–229.

Owe, M., de Jeu, R., Walker, J., 2001. A methodology for surface soil moisture and vegetation optical depth retrieval using the microwave polarization difference index. IEEE Trans. Geosci. Remote Sens. 39 (8), 1643–1654.

Owe, M., de Jeu, R., Holmes, T., 2008. Multisensor historical climatology of satellite-derived global land surface moisture. J. Geophys. Res. Earth Surf. (2003–2012), 113 (F01002).

Parinussa, R.M., Meesters, A.G.C.A., Liu, Y., Dorigo, W., Wagner, W., De Jeu, R.A.M., 2011. Error estimates for near-real-time satellite soil moisture as derived from the land parameter retrieval model. IEEE Geosci. Remote Sens. Lett. 8 (4), 779–783.

Prigent, C., Aires, F., Rossow, W.B., 2006. Land surface microwave emissivities over the globe for a decade. Bull. Am. Meteorol. Soc. 87 (11), 1573–1584.

Rebel, K., De Jeu, R., Ciais, P., Viovy, N., Piao, S., Kiely, G., Dolman, A., 2012. A global analysis of soil moisture derived from satellite observations and a land surface model. Hydrol. Earth Syst. Sci. 16, 833–847.

Reichle, R.H., Koster, R.D., 2005. Global assimilation of satellite surface soil moisture retrievals into the NASA catchment land surface model. Geophys. Res. Lett. 32 (2), L02404.

Reichle, R.H., Koster, R.D., Dong, J., Berg, A.A., 2004. Global soil moisture from satellite observations, land surface models, and ground data: implications for data assimilation. J. Hydrometeorol. 5 (3), 430–442.

Reichle, R.H., Koster, R.D., Liu, P., Mahanama, S.P., Njoku, E.G., Owe, M., 2007. Comparison and assimilation of global soil moisture retrievals from the Advanced Microwave Scanning Radiometer for the Earth Observing System (AMSR-E) and the Scanning Multichannel Microwave Radiometer (SMMR). J. Geophys. Res.-Atmos. 112 (D9), 9108.

Scargle, J.D., 1982. Studies in astronomical time series analysis. II-statistical aspects of spectral analysis of unevenly spaced data. Astrophys. J. 263, 835–853.

Scharlemann, J.P., Benz, D., Hay, S.I., Purse, B.V., Tatem, A.J., Wint, G.W., Rogers, D.J., 2008. Global data for ecology and epidemiology: a novel algorithm for temporal Fourier processing MODIS data. PLoS One 3 (1), e1408.

Seneviratne, S.I., Corti, T., Davin, E.L., Hirschi, M., Jaeger, E.B., Lehner, I., Orlowsky, B., Teuling, A.J., 2010. Investigating soil moisture-climate interactions in a changing climate: a review. Earth-Sci. Rev. 99 (3), 125–161.

Srivastava, P.K., Han, D., Ramirez, M.A.R., Islam, T., 2013. Appraisal of SMOS soil moisture at a catchment scale in a temperate maritime climate. J. Hydrol. 498, 292–304.

Su, C.H., Narsey, S.Y., Gruber, A., Xaver, A., Chung, D., Ryu, D., Wagner, W., 2015. Evaluation of post-retrieval de-noising of active and passive microwave satellite soil moisture. Remote Sens. Environ. 163, 127–139.

Su, C.H., Ryu, D., Western, A.W., Wagner, W., 2013a. De-noising of passive and active microwave satellite soil moisture time series. Geophys. Res. Lett. 40 (14), 3624–3630.

Su, C.H., Ryu, D., Young, R.I., Western, A.W., Wagner, W., 2013b. Inter-comparison of microwave satellite soil moisture retrievals over the Murrumbidgee Basin, southeast Australia. Remote Sens. Environ. 134, 1–11.

Van der Schalie, R., Kerr, Y., Wigneron, J., Rodríguez-Fernández, N., Al-Yaari, A., de Jeu, R., 2016. Global SMOS soil moisture retrievals from the land parameter retrieval model. Int. J. Appl. Earth Obs. Geoinf. 45, 125–134.

Van der Schalie, R., Parinussa, R., Renzullo, L.J., Van Dijk, A., Su, C.-H., de Jeu, R.A., 2015. SMOS soil moisture retrievals using the land parameter retrieval model: evaluation over the Murrumbidgee catchment, southeast Australia. Remote Sens. Environ. 163, 70–79.

Wagner, W., Blöschl, G., Pampaloni, P., Calvet, J.C., Bizzarri, B., Wigneron, J.P., Kerr, Y., 2007a. Operational readiness of microwave remote sensing of soil moisture for hydrologic applications. Hydrol. Res. 38 (1), 1–20.

Wagner, W., Naeimi, V., Scipal, K., de Jeu, R., Martínez-Fernández, J., 2007b. Soil moisture from operational meteorological satellites. Hydrogeol. J. 15 (1), 121–131.

Walker, J.P., Houser, P.R., 2004. Requirements of a global near-surface soil moisture satellite mission: accuracy, repeat time, and spatial resolution. Adv. Water Resour. 27 (8), 785–801.

Wang, G., Garcia, D., Liu, Y., de Jeu, R., Dolman, A.J., 2012. A three-dimensional gap filling method for large geophysical datasets: application to global satellite soil moisture observations. Environ. Model. Softw. 30, 139–142.

Wang, J., Choudhury, B., 1981. Remote sensing of soil moisture content, over bare field at 1.4 GHz frequency. J. Geophys. Res. Oceans 86 (C6), 5277–5282.

Wang, J.R., Schmugge, T.J., 1980. An empirical model for the complex dielectric permittivity of soils as a function of water content. IEEE Trans. Geosci. Remote Sens. 4 (GE-18), 288–295.

Weng, F., 2010. Observations and simulations of microwave land emissivity. In: European Centre for Medium-Range Weather Forecasts — Joint Center for Satellite Data Assimilation (ECMWF—JCSDA) Workshop, June 15–17, Reading, UK.

Wu, W., Dickinson, R.E., 2004. Time scales of layered soil moisture memory in the context of land-atmosphere interaction. J. Clim. 17 (14), 2752–2764.